

# A *Spitzer* mid-infrared spectral survey of mass-losing carbon stars in the Large Magellanic Cloud

Albert A. Zijlstra,<sup>1\*</sup> Mikako Matsuura,<sup>1,2</sup> Peter R. Wood,<sup>3</sup> G. C. Sloan,<sup>4</sup> Eric Lagadec,<sup>1</sup> Jacco Th. van Loon,<sup>5</sup> M. A. T. Groenewegen,<sup>6</sup> M. W. Feast,<sup>7</sup> J. W. Menzies,<sup>8</sup> P. A. Whitelock,<sup>7,8</sup> J. A. D. L. Blommaert,<sup>6</sup> M.-R. L. Cioni,<sup>9</sup> H. J. Habing,<sup>10</sup> S. Hony,<sup>6</sup> C. Loup<sup>11</sup> and L. B. F. M. Waters<sup>12</sup>

<sup>1</sup>University of Manchester, School of Physics & Astronomy, PO Box 88, Manchester M60 1QD

<sup>2</sup>Department of Pure and Applied Physics, The Queen's University of Belfast, Belfast BT7 1NN

<sup>3</sup>Research School of Astronomy and Astrophysics, Australian National University, Cotter Road, Weston Creek, ACT 2611, Australia

<sup>4</sup>Department of Astronomy, Cornell University, 108 Space Sciences Building, Ithaca, NY 14853-6801, USA

<sup>5</sup>Astrophysics Group, School of Physical & Geographical Sciences, Keele University, Staffordshire ST5 5BG

<sup>6</sup>Instituut voor Sterrenkunde, K.U. Leuven, Celestijnenlaan 200B, B-3001 Leuven, Belgium

<sup>7</sup>Department of Astronomy and University of Cape Town, 7701 Rondebosch, South Africa

<sup>8</sup>Department of Mathematics and Applied Mathematics, University of Cape Town, Private Bag, Rondebosch 7701, South Africa

<sup>9</sup>Institute for Astronomy, University of Edinburgh, Royal Observatory, Blackford Hill, Edinburgh EH9 3HJ

<sup>10</sup>Sterrewacht Leiden, Niels Bohrweg 2, 2333 RA Leiden, the Netherlands

<sup>11</sup>Institut d'Astrophysique de Paris, CNRS, 98bis Boulevard Arago, 75014 Paris, France

<sup>12</sup>Astronomical Institute, University of Amsterdam, Kruislaan 403, 1098 SJ Amsterdam, the Netherlands

Accepted 2006 May 25. Received 2006 May 25; in original form 2006 February 10

## ABSTRACT

We present a *Spitzer Space Telescope* spectroscopic survey of mass-losing carbon stars (and one oxygen-rich star) in the Large Magellanic Cloud (LMC). The stars represent the superwind phase on the asymptotic giant branch (AGB), which forms a major source of dust for the interstellar medium (ISM) in galaxies. Bolometric magnitudes indicate progenitor masses of 1.5–2.5  $M_{\odot}$ . The spectra cover the wavelength range 5–38  $\mu\text{m}$ . They show varying combinations of dust continuum, dust emission features (SiC, MgS) and molecular absorption bands ( $\text{C}_2\text{H}_2$ , HCN). A 10- $\mu\text{m}$  absorption feature is attributed to  $\text{C}_3$ . A weak band at 5.8  $\mu\text{m}$  is suggestive of carbonyl. The circumstellar 7.5- $\mu\text{m}$   $\text{C}_2\text{H}_2$  band is found to be stronger at lower metallicity, explained by higher C/O ratios at low metallicity. The  $J - K$  versus  $K - A$  colours, used to select the sample, are shown to be relatively insensitive in separating carbon versus oxygen-rich AGB stars. The predominance of carbon stars therefore indicates that in the range 1.5–2.5  $M_{\odot}$ , LMC AGB stars become carbon-rich before onset of the superwind. A set of four narrow bands, dubbed the Manchester system, is used to define the infrared continuum for dusty carbon stars. We investigate the strength and central wavelength of the SiC and MgS dust bands as a function of colour and metallicity. The line-to-continuum ratio of these bands shows some indication of being lower at low metallicity. The MgS band is only seen at dust temperatures below 600 K. Metal-poor carbon stars can form amorphous carbon dust from self-produced carbon. The formation efficiency of oxygen-rich dust depends more strongly on metallicity. In lower-metallicity environments, the dust input into the ISM by AGB stars may be strongly biased towards carbonaceous dust.

**Key words:** stars: AGB and post-AGB – stars: carbon – stars: mass-loss – Magellanic Clouds.

## 1 INTRODUCTION

Low- and intermediate-mass stars ( $M \sim 1\text{--}8 M_{\odot}$ , hereafter LIMS) make up >90 per cent of all the stars which have died in the Universe up to the present time. During their late evolution, after entering the

\*E-mail: a.zijlstra@manchester.ac.uk

high-luminosity asymptotic giant branch (AGB) phase, the stars eject their hydrogen-rich outer layers during a phase of catastrophic mass-loss: the so-called superwind phase. After this final burst of activity, the star remains as a hot, compact white dwarf of mass 0.6–1.4  $M_{\odot}$ . The expanding ejecta surrounding the star become ionized and form a planetary nebula, before dispersing into the interstellar medium (ISM).

The superwind is here defined as the phase when the mass-loss rate exceeds the nuclear-burning rate and mass-loss dominates the evolution (Willson 2000). During the superwind, the mass-loss rate increases from  $\sim 10^{-6} M_{\odot} \text{ yr}^{-1}$  to  $\sim 10^{-4} M_{\odot} \text{ yr}^{-1}$  (Vassiliadis & Wood 1993; Bloeker 1995); the star becomes self-obscured by dust which forms in the ejecta. Dredge-up of primary carbon (produced by triple- $\alpha$  burning) may turn the star into a carbon star. The ejecta are largely molecular. The first and most stable molecule to form is CO: this locks up the least abundant of the C and O atoms. Other molecules and dust form from the remaining atoms. The chemistry changes dramatically as the C/O ratio (by number) passes unity, and this affects both the gas-phase species (Willacy & Millar 1997; Millar, Herbst & Bettens 2000) and the dust composition (Treffers & Cohen 1974). In carbon stars, the C/O ratio exceeds unity, and carbon-rich molecules (e.g.  $\text{C}_2\text{H}_2$ , HCN) and carbonaceous dust (Hony 2002) result, whilst in oxygen stars (C/O < 1), metal oxides and silicate dust (Cami 2002) form. The intermediate SC stars show little dust formation (Zijlstra et al. 2004).

The mass-loss process is important for three reasons. First, it determines the mass distribution of stellar remnants, including, e.g. the lower mass limit of type II supernovae progenitors (Zijlstra 2004). Secondly, the physics and interplay of stellar pulsation, shock waves, dust formation and radiation pressure which drives the mass-loss are still little understood. Thirdly, stellar mass-loss drives Galactic evolution through replenishment and enrichment of the ISM. On this last point, mass-loss from LIMS contributes roughly half the total gas recycled by all stars (Maeder 1992), creates an amount of carbon roughly equal to that produced by supernovae and Wolf–Rayet stars (Dray et al. 2003; Gavilán, Buell & Mollá 2005) and is the main source of carbonaceous interstellar dust (Dwek 1998; Edmunds 2001). LIMS are the only confirmed source of the primary nitrogen required to explain observed abundances in objects in the early Universe. AGB and post-AGB stars are the main sources of  $^{13}\text{C}$  (Hajduk et al. 2005) and heavy s-process elements (Goriely & Mowlavi 2000; Wanajo et al. 2006). LIMS are the major stellar source of lithium (Romano et al. 2001; Travaglio et al. 2001).

The AGB and post-AGB evolution is dominated by the superwind mass loss. Theoretical models (e.g. Sandin & Höfner 2003) cannot yet predict mass-loss rates from stellar parameters: instead observational knowledge is required of the mass-loss rates as a function of mass, luminosity and metallicity. However, the observational relations are themselves not well calibrated: local Galactic stars have poorly known distances and unknown progenitor masses, while extragalactic stars are in general too faint to detect the mass-loss tracers. Important work has been carried out on bulge stars (Ortiz et al. 2002). The main tracer for the superwind is the dust, which emits in the thermal infrared (IR). Surveys by the *Infrared Astronomical Satellite* (IRAS) uncovered a number of luminous self-obscured AGB stars in the Magellanic Clouds (Reid 1991; Zijlstra et al. 1996). The *Infrared Space Observatory* (ISO) made it possible to measure their mass-loss rates, but only for the most massive stars and the highest mass-loss rates (e.g. van Loon et al. 1999a). A larger number of these stars was discovered more recently with the Mid-course Space Experiment (MSX) satellite (Egan, Van Dyk & Price 2001).

The *Spitzer Space Telescope* (Werner et al. 2004) for the first time provides the sensitivity necessary to obtain mass-loss rates for the whole range of AGB masses and luminosities in the Magellanic Clouds. These stars have well-known distances, meaning that absolute luminosities can be easily obtained. The general abundance of field stars may be estimated from the well-studied age–metallicity relations, and abundances have been derived explicitly for many star clusters. We have thus undertaken a survey of stars all along the AGB in the Large Magellanic Cloud and the Small Magellanic Cloud (hereafter LMC and SMC, respectively) with *Spitzer*. In this paper we present the LMC stars observed in our survey. Data for the SMC stars and the analysis of mass-loss rates will appear in subsequent papers.

## 2 TARGET SELECTION

The ( $M_K$ ,  $J - K$ ) diagram in Fig. 1(a) shows most of the AGB stars which are known to be mid-IR point sources in the LMC. Also shown is a representative sample of the much more numerous field stars without thick dust shells. The most numerous stars in any stellar population are low-mass stars. In Fig. 1(a), these stars evolve up the AGB in  $M_K$  at  $J - K < 2.5$  and  $M_K > -9$ , before they develop high mass-loss rates and thick dust shells and evolve to  $J - K \sim 7$  and  $M_K \sim -5$ . Fig. 1(a) also includes massive AGB stars ( $M > 3 M_{\odot}$ ,  $-10.5 < M_K < -9$ ), deriving from intermediate-mass progenitor stars.

Stars observed in the current survey are shown in Fig. 1(b). We selected targets in both the SMC and the LMC from the MSX catalogue (Egan et al. 2001), the *IRAS* point source catalogue, the *ISO* catalogue of variable AGB stars in the SMC (Cioni et al. 2003), long-period variables (LPVs) in the Magellanic Clouds (e.g. Wood, Bessell & Fox 1983; Feast et al. 1989), and the intermediate-age clusters NGC 419 and 1978, both of which have a known mid-IR source. Targets were selected to span the long sequence of increasing mass-loss in LIMS which stretches from ( $J - K$ ,  $M_K$ )  $\sim$  (2,  $-9$ ) to (7,  $-4$ ) in Fig. 1(a). [The bright oxygen-rich object near ( $J - K$ ,  $M_K$ )  $\sim$  (1,  $-10.7$ ) in Fig. 1(b) was not a target but was accidentally observed when *Spitzer* selected it in the peak-up field.] It turns out that only two of the LMC sources were oxygen-rich, one of which was found to be a massive young stellar object (van Loon et al. 2005b). Here we present the remaining sources in the LMC. The SMC sample will be presented elsewhere.

Table 1 lists the 29 stars included here. The objects have been included in various catalogues over time, accumulating different names. We adopt the oldest available name for each object, but Table 1 gives the cross-references to names used by Reid, Tinney & Mould (1990), Egan et al. (2001) and in the MSX catalogue. The adopted positions are from two-Micron All-Sky Survey (2MASS) counterparts and differ slightly from the MSX positions.

The  $JHK_s$  photometry in Table 1 is taken from the 2MASS catalogue. It is based on a single epoch only and does not sample the variability. Where further data are available, we list  $JHKL$  photometry averaged over the cycle in Table 2. Also listed are pulsation periods, taken from Whitelock et al. (2003), Wood (1998), Nishida et al. (2000), Ita et al. (2004) and Groenewegen (2004). Where available, periods from Whitelock et al. (2003) are listed in preference because of the larger number of observations used. Photometry is taken from the first three references, with values from Wood (1998) listed preferably, where available. Especially the  $L$ -band filters differ substantially between the sources; the photometry is in the original system. For MSX LMC 967, the photometry is an average of two

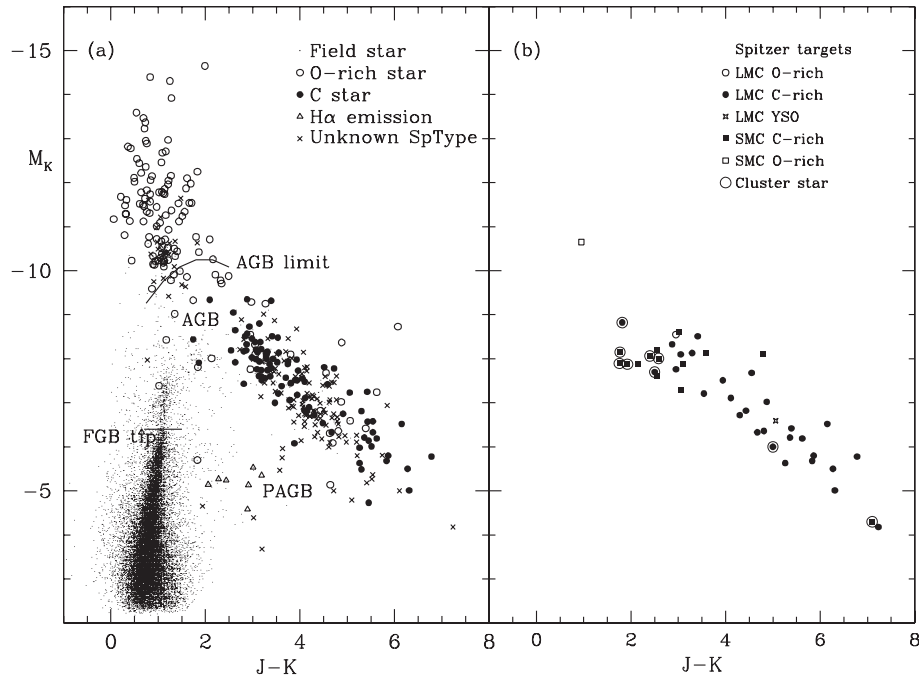


**Figure 1.** (a) The  $M_K, J - K$  diagram for a sample of known mid-IR sources (MSX and *IRAS*) in the LMC (large points), together with field stars (small symbols) from an area  $\sim 60$  times smaller than the area from which the mid-IR sources were selected. AGB stars are confined approximately to the region below the line marked ‘AGB limit’. Stars above this limit are foreground stars and supergiants: the supergiant stars have masses  $M > 8 M_{\odot}$ . Spectral types were those available before the *Spitzer* observations were made (b) similar to (a), except that the objects shown are the point sources actually observed, and the spectral types come from recent ground-based and *Spitzer* spectra. In both panels, distance moduli of 18.5 and 18.9 have been assumed for the LMC and SMC, respectively.  $J$  and  $K$  photometry is from various sources existing prior to the *Spitzer* observations.

observations only: 2MASS and a single measurement from Ita et al. (2004).

Fig. 2 shows the  $M_K$  versus  $J - K$  colour–magnitude diagram, using photometry listed above supplemented with data from van Loon et al. (2006). The stars follow the line of increasing mass-loss defined in Fig. 1(a). Neither figure includes the stars which are faintest at  $K$ , as these show only upper limits for  $J$ .

## 2.1 Comments on individual stars

Three stars in Table 1 are located in the cluster NGC 1978, as indicated by their names. The cluster was studied by Tanabé et al. (1997); it has an age of  $2.5 \times 10^9$  yr, a turn-off mass of about  $1.5 M_{\odot}$  and a metallicity  $[\text{Fe}/\text{H}] = -0.66 \pm 0.22$  (van Loon, Marshall & Zijlstra 2005a). One star, MIR-1, is a known obscured LPV, one other is an MSX-detected star, and the third (IR4, Will et al. 1995; van Loon et al. 2005a) is an AGB star with no listed MSX point-source counterpart. This last star is seen on MSX images, from which van Loon et al. (2005a) estimate a flux density of 70 mJy in MSX band A (6.8–10.8  $\mu\text{m}$ ).

*IRAS* 04557–6753 is also located in a (small) cluster, KMHK 285 (Bica et al. 1999; van Loon et al. 2005a), but this cluster is little studied. The age is estimated as  $> 10^9$  yr and the metallicity is not known.

MSX LMC 494 is identified with a large amplitude variable observed with the Optical Gravitational Lensing Experiment, OGLE 052309.18–691747.0.

LMC MSX 663 is also a long-period OGLE variable but its OGLE amplitude is very small (Groenewegen 2004). It is an optically bright AGB star previously classified as an S star (Cioni et al. 2001). How-

ever, optical spectra show that it is a symbiotic carbon star with strong emission lines (Wood et al. in preparation).

*IRAS* 05291–6700 was identified with a nearby variable star, GRRV 38 (Glass & Reid 1985), but the coordinates of the *IRAS* source differ by 30 arcsec from this star. The identification of the star (Zijlstra et al. 1996) most likely occurred serendipitously; the *IRAS* point source is likely unrelated. There is confusion with an extended mid-IR source approximately 6 arcmin east. MSX only shows the stellar source, but nothing at the position of the *IRAS* source. GRRV 38 is a carbon star (van Loon, Zijlstra & Groenewegen 1999b); the IR colours indicate little or no obscuration. Below we will use the name GRRV 38 for this object.

For TRM 88, Wood (1998) and Whitelock et al. (2003) report main periods of 565 and 544 d, respectively. The light curve is affected by long-term secular changes (Whitelock et al. 2003) due to variable circumstellar extinction (Feast, Whitelock & Marang 2003).

*IRAS* 05009–6616 and TRM 72 also show evidence for long-term variations in the light curves (Whitelock et al. 2003). TRM 72 should not be confused with the well-studied CH star WORC 106 (Feast & Whitelock 1992) which is located 30 arcsec away.

## 3 OBSERVATIONS

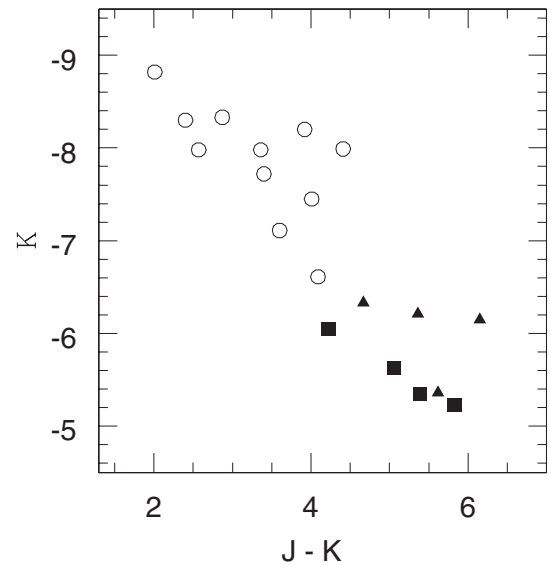
We observed our targets with the Infrared Spectrograph (IRS) (Houck et al. 2004) on the *Spitzer Space Telescope* using the low-resolution modules short-low (SL) and long-low (LL), which together cover wavelengths from 5 to 38  $\mu\text{m}$ . The slits in SL are roughly perpendicular to LL, and each module has two separate apertures, with the longer wavelengths observed in first order and the lower in second order. In order of increasing wavelength, the four

**Table 1.** Observed LMC targets: names, adopted coordinates and photometry. The MSX photometry is for band *A* (8.2  $\mu\text{m}$ ) and refers to version 2.3 of the catalogue. The zero-point for the MSX band *A* is taken as 58.46 Jy (Egan et al. 2001). *JHK* is taken from 2MASS, except for MSX LMC 494 and NGC 1978 MIR1 where the values are from Ita et al. (2004) and van Loon et al. (2005a), respectively.  $M_{\text{bol}}$  (Section 3.1) assumes a distance modulus of 18.5.

Adopted name	MSX source	Other name	Right ascension (J2000)	Declination	<i>J</i> (mag)	<i>H</i> (mag)	<i>K<sub>s</sub></i> (mag)	<i>A</i> (mJy)	$M_{\text{bol}}$
Carbon-rich									
MSX LMC 219	051119.5–684227		05 11 19.52	–68 42 27.9	>15.61	>14.67	13.14	204	–4.76
IRAS 05132–6941	051250.8–693749	MSX LMC 223	05 12 51.07	–69 37 50.3	>17.81	>15.68	13.36	259	–5.01
MSX LMC 349	051726.9–685458		05 17 26.94	–68 54 58.2	>17.44	>16.88	14.82	193	–4.97
MSX LMC 341	052100.5–692054		05 21 00.37	–69 20 55.3	>17.49	15.9:	13.151	210	–4.74
MSX LMC 663	052244.5–693826		05 22 44.00	–69 38 28.1	12.60	11.33	10.20	75	–5.40
MSX LMC 494	052309.6–691744		05 23 09.11	–69 17 49.1	13.08	11.71	10.51	94	–4.98
MSX LMC 441	052438.7–702357		05 24 38.62	–70 23 57.1	>17.16	>16.44	14.48	200	–4.92
MSX LMC 443	052505.9–701011		05 25 05.69	–70 10 10.6	>14.54	13.72	11.54	150	–4.68
MSX LMC 601	052650.9–693136		05 26 50.83	–69 31 36.9	13.88	11.99	10.52	172	–5.14
NGC 1978 IR4		WBT 815	05 28 44.50	–66 14 04.0	11.49:	10.34:	9.68	70:	–5.35
NGC 1978 MIR1			05 28 47.20	–66 14 13.6	16.67		12.45	124	–4.75
NGC 1978 IR1		WBT 1268	05 28 40.17	–66 13 54.2	>13.78	>12.78	11.73	77	–5.03
IRAS 05278–6942	052724.3–693944	MSX LMC 635	05 27 24.12	–69 39 45.0	>17.53	>15.59	12.35	683	–6.57
MSX LMC 754	052811.4–703359		05 28 11.48	–70 33 58.7	15.98:	13.70	11.89	93:	–4.91
MSX LMC 679	052848.5–694801		05 28 48.62	–69 48 01.3	>15.84	14.57	12.48	121	–4.93
MSX LMC 743	053454.1–702925		05 34 53.74	–70 29 24.8	>14.13	>13.22	13.27	165	–5.27
MSX LMC 749	053527.1–695229		05 35 26.86	–69 52 27.9	15.06	12.93	11.05	142	–5.56
MSX LMC 967	053637.2–694725		05 36 36.71	–69 47 22.6	13.48	12.00	10.67	87:	–5.45
IRAS 04557–6753		MSX LMC 1238	04 55 38.98	–67 49 10.7	>16.18	14.49	12.397	157	–5.05
IRAS 05009–6616		MSX LMC 1278	05 01 04.43	–66 12 40.4	>15.64	14.57	12.40	240	–5.57
IRAS 05291–6700		GRRV 38	05 29 07.60	–66 58 15.0	12.45	10.91	9.91	81:	–4.91
IRAS 05295–7121		MSX LMC 692	05 28 46.62	–71 19 12.5	16.80:	14.32	12.18	204	–5.24
TRM 88		MSX LMC 310	05 20 19.38	–66 35 47.8	14.76	12.81	11.10	169	–5.15
IRAS 05112–6755		MSX LMC 44, TRM 4	05 11 10.47	–67 52 10.5	16.41:	14.07	11.69	451	–5.59
IRAS 05190–6748		MSX LMC 307, TRM 20	05 18 56.26	–67 45 04.4	>18.21	>15.91	13.10	209	–5.61
IRAS 05113–6739		MSX LMC 47, TRM 24	05 11 13.89	–67 36 16.1	>17.72	14.77	12.49	233	–5.18
TRM 72		MSX LMC 29	05 11 38.65	–66 51 09.8	14.34	12.36	10.74	122	–5.43
IRAS 05360–6648		MSX LMC 872, TRM 77	05 36 01.24	–66 46 39.7	>18.04	16.07:	13.28	192	–4.73
Oxygen-rich									
IRAS 05003–6712		MSX LMC 1280	05 00 19.00	–67 07 58.0	12.04	10.46	9.32	205	–5.42

**Table 2.** Phase-averaged photometry and periods. Periods are taken from Whitelock et al. (2003), Wood (1998), Nishida et al. (2000) and Groenewegen (2004).

Adopted name	<i>J</i> (mag)	<i>H</i> (mag)	<i>K</i> (mag)	<i>L</i> (mag)	<i>P</i> (d)
MSX LMC 663					455:
MSX LMC 494					458
MSX LMC 601					546
NGC 1978 IR1	14.26	12.01	10.51	–	491
MSX LMC 749					329, 589
MSX LMC 967	(14.2)	(12.5)	(10.8)	–	572
IRAS 04557–6753		13.97	11.78	9.11	765
IRAS 05009–6616		13.06	11.29	8.94	658
GRRV 38	13.04	11.33	10.17	8.86	483
IRAS 05295–7121		12.96	10.99	8.83	682
TRM 88	14.22	12.10	10.30	8.26	544
IRAS 05112–6755	17.65	15.11	12.29	8.89	830
IRAS 05190–6748		16.11	12.72	8.71	939
IRAS 05113–6739	16.84	14.63	12.17	8.93	700
TRM 72	15.50	13.33	11.39	8.92	631
IRAS 05360–6648		15.50	12.87	9.24	538
IRAS 05003–6712	12.90	11.26	9.95	8.49	883

**Figure 2.** The  $M_K$ ,  $J - K$  diagram for the sources in this paper.  $J$  and  $K$  values are taken from Tables 1 and 2, and from van Loon et al. (2005a). Objects with lower limits only for the  $J - K$  colour are not included. Symbols indicate a source classification based on data described in this paper: open circles—stars without a MgS feature; triangles—a weak SiC features and MgS; filled squares—strong SiC and MgS.

spectral segments are known as SL2, SL1, LL2 and LL1. In addition, a ‘bonus’ order covers the overlap between the first and second orders in each module; this order is a small piece of the first-order spectrum obtained when the source is in the second-order aperture. When the source is in one aperture, the other aperture is exposed to a section of nearby sky, providing a background measurement, e.g. in SL2 when the source is in the SL1 aperture. Each source was observed in two nod positions in each aperture. The resolution varies between 64 and 128, depending on the order and wavelength. The slit dimensions are approximately  $3.5 \times 57$  arcsec<sup>2</sup> for SL and  $10.5 \times 168$  arcsec<sup>2</sup> for LL (width  $\times$  length).

Different exposure times were used depending on expected target flux. For SL, 12- to 120-s exposure times were used per spectral segment. For LL1, exposure times ranged from 60 to 960 s, and for LL2 from 180 to 960 s. Observations were taken in standard staring mode.

Flat-fielded images were generated by the *Spitzer* Science Centre (SSC). We replaced bad pixels with values estimated from neighbouring pixels (using the IMCLEAN.PRO package), and removed the background emission by differencing images aperture-by-aperture in SL (e.g. SL1–SL2 and vice versa), and nod-by-nod in LL. Spectra were extracted from the images using the software provided with the *Spitzer* IRS Custom Extractor (SPICE) available from the SSC. They were calibrated making a full spectral correction using HR 6348 (K0 III) as a standard star in SL and HR 6348, HD 166780 (K4 III), and HD 173511 (K5 III) in LL. Individual images were extracted separately and then co-added. Nods were combined, then spectral segments were combined by making scalar multiplicative corrections for pointing-induced throughput errors (normalizing to the best-centred segment). The accuracy of the overall spectral shape is limited to a few per cent. The matching across the different sections (e.g. LL2 to LL1) may leave some residuals.

The standard wavelength calibration is accurate to better than 0.06  $\mu\text{m}$  in SL and 0.15  $\mu\text{m}$  in LL. Flux calibration is accurate to  $\lesssim 5$  per cent. The response curve is known to a few per cent, but residuals at this level may remain. The largest residual calibration errors are due to pointing uncertainties. The LL array is affected by fringing which in most cases has been corrected. Sloan, Nerenberg & Russell (2003) discuss the calibration issues in more detail.

Fig. 3 show the spectra of the carbon stars. They are ordered by dust temperature, from blue spectra to red. The spectra show numerous absorption and emission bands of molecules and dust resonances, superposed on the dust continuum. One star is included twice: it was accidentally re-observed. We will first discuss these bands, separated into dust and molecular features. The following section will discuss the continuum spectral energy distribution.

Some objects show residual interstellar lines, due to incomplete cancellation of the background emission. These lines are found at 33.5  $\mu\text{m}$  ([S III]), 34.8  $\mu\text{m}$  ([Si II]), and 36.0  $\mu\text{m}$  ([Ne III]). An apparent feature at 30.5  $\mu\text{m}$  seen in a few spectra is an artefact, due to a hot pixel.

The object MSX LMC 663 exhibits an IRS spectrum which is very different from the others, as Fig. 4 shows. It is affected by interstellar emission in the background measurement, causing the offset measurements to disagree; however, the rise beyond 25  $\mu\text{m}$  appears to be intrinsic to the star and not due to background emission. Shortward, the spectrum shows little evidence for dust but the absorption bands are different in shape from those of the other carbon stars.

The best example of a naked carbon star is NGC 1978 IR4, which has the bluest mid-IR spectrum. This object was observed twice. Fig. 5 shows the averaged spectrum. It shows some noticeable dif-

ferences with the other stars: the 5- $\mu\text{m}$  absorption is very deep, and an absorption feature is apparent between 8.5 and 11  $\mu\text{m}$ .

IRAS 05003–6712 (Fig. 6) is the only oxygen-rich AGB star in our sample (one other object was classified as a massive young stellar object, and is published by van Loon et al. 2005b). It has an OH maser (Marshall et al. 2004), but only the blue-shifted component is detected. The silicate emission features at 10 and 18  $\mu\text{m}$  dominate the *Spitzer* spectrum. The 10- $\mu\text{m}$  feature is typical for a lower mass-loss rate: it is comparable to that of the LMC AGB star IRAS 04544–6849 (Dijkstra et al. 2005) with a mass-loss rate of  $\dot{M} = 7 \times 10^{-6} M_{\odot} \text{yr}^{-1}$  (van Loon et al. 1999a). There is some evidence for crystalline silicate features. These are unusual in a star with a relatively low-dust mass-loss rate (Kemper et al. 2001). Warm crystalline silicates have also been seen in the LMC star HV 2310 (Sloan et al. 2006a).

### 3.1 Bolometric magnitudes

For a number of our targets, Wood (1998) and Whitelock et al. (2003) have derived bolometric magnitudes. Table 1 lists the bolometric magnitudes derived from the *Spitzer* spectra and *JHK<sub>s</sub>* 2MASS photometry. Where multi-epoch photometry was available (Table 2), those were used instead of the single-epoch 2MASS data. The spectra were smoothed by a factor of 20. The *J*-band upper limit was used as a real magnitude where necessary: this has no measurable effect on the result (changing it by 1 mag affected the bolometric flux by less than 1 per cent). Zero flux was assumed at frequencies of 0 and  $3 \times 10^{16}$  Hz (100 Å). A fourth-order polynomial was fitted (using IDL) to the spectra and data points and the total flux was obtained by integration under the fit. For the blue carbon stars, a small uncertainty is introduced by the lack of data points between 2 and 5  $\mu\text{m}$ . The distance modulus introduces an uncertainty of 0.1 mag. Variability is the main limitation to the accuracy: the *K*-band magnitude can vary by up to 1–2 mag in the extreme cases (Le Bertre 1992; Wood 1998; Whitelock et al. 2003). As the amplitudes are not known for our sample, the accuracy is uncertain. We attribute a tentative uncertainty  $\sigma = 0.2$  mag.

The result was converted to absolute magnitude assuming a distance modulus of 18.5 (e.g. Alves et al. 2002). The distance modulus varies by approximately 0.1 mag over the face of the bar (Lah, Kiss & Bedding 2005) but we did not correct for such geometric effects.

Fig. 7 shows a histogram of the bolometric magnitudes. Comparing the  $M_{\text{bol}}$  values in this figure with the  $M_{\text{bol}}$  values of the high mass-loss rate stars in fig. 20 of Vassiliadis & Wood (1993) suggests that the objects we have observed with *Spitzer* are predominantly in the initial mass range 1.5–2.5  $M_{\odot}$ .

## 4 EMISSION AND ABSORPTION BANDS

### 4.1 Dust features

Carbon stars show two major dust features in this spectral region, at 11.3 and 30  $\mu\text{m}$ . Both features are seen in the majority of the current sample, although not in all. Two other spectral features have been suggested as being due to dust, but below we argue against this possibility.

#### 4.1.1 SiC dust emission

The well-known 11.3- $\mu\text{m}$  feature is due to solid  $\alpha$ -SiC (e.g. Papoular et al. 1998; Clément et al. 2003). The central wavelength shows some

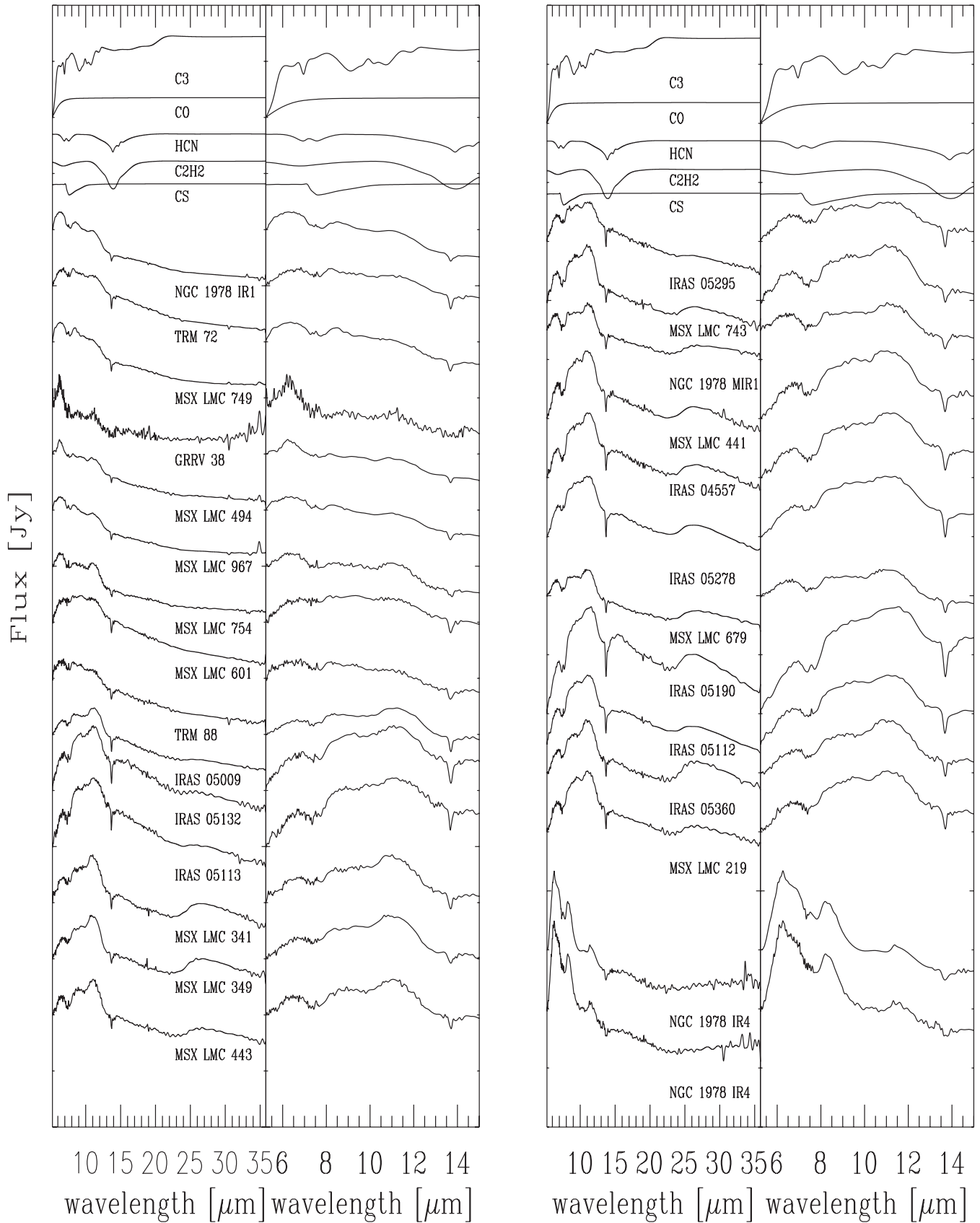


**Figure 3.** Spectra of the carbon-rich AGB stars observed in the LMC. The top five lines show the model molecular spectra for TT Cyg from Jørgensen et al. (2000). Left-hand panel: bluer spectra; right-hand panel: 11 redder carbon-rich AGB stars and spectra of the blue ('naked') carbon star NGC 1978 IR4 which was observed twice.

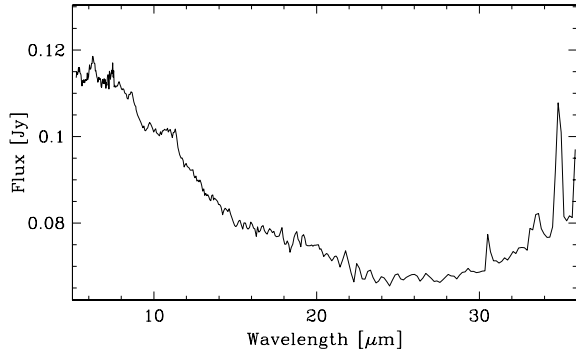


**Figure 4.** Spectrum of the symbiotic C star MSX LMC 663

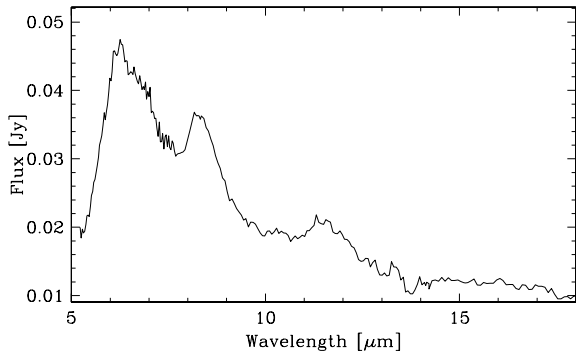


**Figure 5.** Spectrum of the ‘naked’ carbon star NGC 1978 IR4.

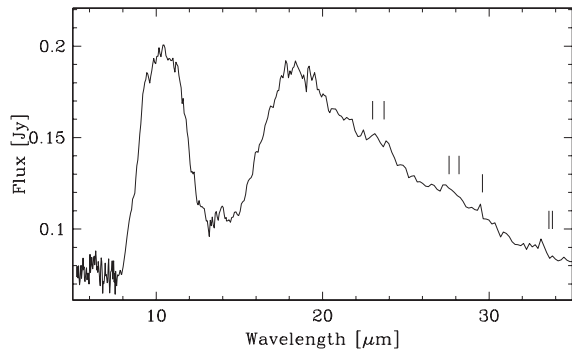


**Figure 6.** Spectrum of the oxygen-rich AGB star IRAS 05003–6712. The vertical bars show the location of crystalline silicate features (Molster, Waters & Tielens 2002): enstatite (23.0, 28.2  $\mu\text{m}$ ) and forsterite (23.7, 27.6, 33.6  $\mu\text{m}$ ); the 29.6 and 33.8  $\mu\text{m}$  are unidentified.

variability in Galactic carbon stars (Speck, Thompson & Hofmeister 2005), ranging between 11.15 and 11.7  $\mu\text{m}$ . Longer wavelengths are correlated with lower dust (continuum) temperatures (Baron et al. 1987). Clément et al. (2003) find that the wavelength shift to the red can be reproduced in SiC particle conglomerates, and they suggest that conglomerates form at higher density in the wind. In this case the correlation with the dust temperature is an indirect one, caused by a larger optical depth in the dust shell.

#### 4.1.2 MgS dust emission

The 30- $\mu\text{m}$  resonance is commonly seen in carbon-rich environments, in AGB stars, post-AGB stars and planetary nebulae (Forrest,

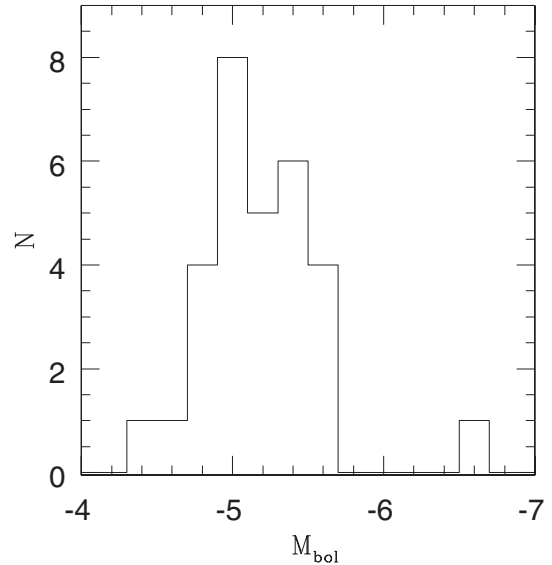


**Figure 7.** Distribution of bolometric magnitudes.

Houck & McCarthy 1981; Hony 2002). It consists of two subpeaks, at 26 and 33  $\mu\text{m}$  (Volk et al. 2002). The two peaks always appear together, arguing for an origin in the same mineral. The resonance is attributed to MgS (Goebel & Moseley 1985) which forms via a grain-surface reaction between Mg and  $\text{H}_2\text{S}$  (Nuth et al. 1985); the two peaks have been attributed to different grain shapes (Hony, Waters & Tielens 2002). A contribution from CaS to the features cannot be fully excluded, but the absence of any feature in oxygen-rich environments argues against this (Goebel & Moseley 1985). The peak wavelength of the MgS feature shifts with temperature, which makes it an important temperature diagnostic (Hony & Bouwman 2004). Hony et al. (2002) argue that solid MgS may survive into the ISM.

#### 4.1.3 Doubtful features

Two objects show indications of a broad, weak hump between 16 and 23  $\mu\text{m}$ , with unclear identification. It is most noticeable in the symbiotic C star LMC MSX 663, and may be seen weakly in MSX LMC 754, a carbon star with hot dust. Neither object shows evidence for MgS. The feature is likely an artefact caused by the broad molecular  $\text{C}_2\text{H}_2$  absorption band to the blue.

A possible emission feature at 8.6  $\mu\text{m}$  has been described in IRAS LRS (Low Resolution Spectrometer) spectra of Galactic carbon stars (Sloan, Little-Marenin & Price 1998; Willems 1988). The feature correlates in strength with the SiC band and the 3  $\mu\text{m}$  band. However, its reality is disputed: strong absorption at 7.5  $\mu\text{m}$  together with 10  $\mu\text{m}$  absorption can mimic an emission band. The spectra in our LMC sample show strong absorption at 7.5  $\mu\text{m}$  and possible absorption at 10  $\mu\text{m}$ , making it more likely that the 8.6  $\mu\text{m}$  peak is simply the continuum between two molecular bands (Aoki, Tsuji & Ohnaka 1999), which we will assume below.

## 4.2 Molecular bands

The molecular bands are at the short wavelength range of the IRS spectra, where the stretching and bending vibrations of single molecules are found. Gautschy-Loidl et al. (2004) discuss the contribution of different molecules to the 5–20- $\mu\text{m}$  wavelength range.

Models for individual bands were calculated by Jørgensen, Hron & Loidl (2000): the top of Fig. 3 shows their models for TT Cyg. (TT Cyg was selected because it has the highest C/O ratio of their three stars, and is therefore most representative of the LMC stars).

#### 4.2.1 13.7 $\mu\text{m}$

The narrow 13.7- $\mu\text{m}$  band is prominent in most of the spectra. This band arises from the Q-branch  $\text{C}_2\text{H}_2$   $\nu_5$  transition (Tsuji 1984; Aoki et al. 1999; Cernicharo et al. 1999). The narrow band is sitting in the much broader P and R branches, giving rise to an absorption feature extending from 12 to 16  $\mu\text{m}$ , which is best seen in the spectrum of IRAS 05190–6748. Models of Galactic carbon stars (Gautschy-Loidl et al. 2004) predict a much stronger broad-band than is observed, which may be explained if the mass-losing envelope adds a molecular emission feature (Aoki et al. 1999) or fills in the feature with dust emission (Jørgensen et al. 2000). The sharp 13.7- $\mu\text{m}$  band is very strong in our spectra, while in Galactic stars it has been dubbed the ‘weak’ feature (Gautschy-Loidl et al. 2004). The sharp feature originates from colder gas, while hot (up to photospheric temperatures) gas mainly shows the broad-band (Jørgensen et al. 2000).

The 11.3- $\mu\text{m}$  SiC emission feature makes it difficult to judge how strong this broad absorption band is. The top panel of Fig. 8 shows an indicative spectrum obtained by averaging the stars without a MgS feature (which also have weak or missing SiC features; see Section 6.4 below), and dividing it by the spectrum of the symbiotic C star LMC MSX 663 which shows at most very weak  $\text{C}_2\text{H}_2$ . A gradient has also been subtracted. The resulting plot indicates that the R branch starts fairly sharply at 12  $\mu\text{m}$ . Some overlap between the  $\text{C}_2\text{H}_2$  and SiC features is possible.

#### 4.2.2 14.3 $\mu\text{m}$

The 14.3- $\mu\text{m}$  HCN band seen in Galactic carbon stars (Aoki et al. 1999; Cernicharo et al. 1999) is weak in our sample. It is probably present in the spectrum of TRM 72. Otherwise the feature is not clear, and is certainly much weaker than the  $\text{C}_2\text{H}_2$  band. This is similar to the situation in Galactic stars, where its weakness is attributed to in-fill by an emission component (Aoki et al. 1999).

#### 4.2.3 7.5 $\mu\text{m}$

A noticeable absorption band is present at 7.5  $\mu\text{m}$ . Galactic carbon stars have contributions in this wavelength region from  $\text{C}_2\text{H}_2$ , HCN and CS (Goebel et al. 1981; Aoki, Tsuji & Ohnaka 1998). The sample of Aoki et al. (1998) consists of blue carbon stars, which differ in effective temperature from our sample.

The shape of the two shallow features found in our spectra resembles  $\text{C}_2\text{H}_2$ . The diatomic molecule CS shows a band head which we do not see, and the HCN band is located at shorter wavelength, typically centred around 7.0  $\mu\text{m}$  (although this central wavelength depends on the excitation temperature). A difference in the shape of the 7.5- $\mu\text{m}$  band supports different origins for Galactic and LMC carbon stars. Matsuura et al. (2002a, 2005) show that at low metallicity,  $\text{C}_2\text{H}_2$  becomes more abundant compared to HCN. Following this, we identify the observed band for LMC stars with  $\text{C}_2\text{H}_2$ .

#### 4.2.4 5 $\mu\text{m}$

At the blue edge of the spectra the spectral energy distributions drop sharply, due to a strong absorption band which extends beyond the blue limit of the wavelength range. There are two molecules which

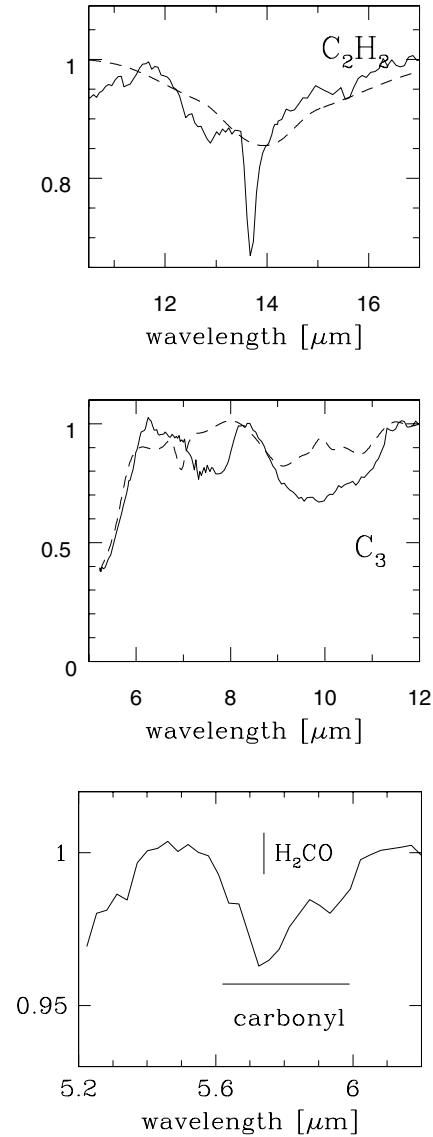


**Figure 8.** Detected bands for three molecules. The spectra have been divided by an estimated continuum. The top panel shows an average of spectra without an MgS feature, divided by the (almost featureless) spectrum of LMC MSX 663. The middle panel shows the (continuum-divided) spectrum of NGC 1978 IR4, with the  $\text{C}_3$  model. The bottom panel shows a (continuum-divided) average of all spectra apart from NGC 1978 IR4 and LMC MSX 663: the weak band is identified with a carbonyl group. The vertical line indicates the central wavelength of formaldehyde ( $\text{H}_2\text{CO}$ ) absorption, while the horizontal line indicates the wavelength range of other possible carbonyl groups.

contribute at this wavelength in carbon-rich environments: CO and  $\text{C}_3$  (Jørgensen et al. 2000). CO originates in the photosphere and is present even in K stars.  $\text{C}_3$  also is photospheric in carbon stars.

The middle panel of Fig. 8 shows the spectrum of NGC 1978 IR4, with an estimate for the continuum subtracted. This star has the bluest *Spitzer* spectrum of our sources and is the best example of a naked carbon star. The  $\text{C}_3$  model provides a good approximation to the observed 5- $\mu\text{m}$  band.

#### 4.2.5 5.8 $\mu\text{m}$

Most of the observed sources show either a change in slope or a weak dip between 5.6 and 6  $\mu\text{m}$ . This is illustrated in the bottom

panels of Fig. 8, which is an average spectrum over all sources except NGC 1978 IR4 and LMC MSX 663. The spectrum has been divided by an estimate for the continuum (the wing of the 5- $\mu\text{m}$  band). A weak absorption band with depth of a few per cent is seen.

The wavelength of this band coincides precisely with the stretching vibration of a carbonyl group ( $1670\text{--}1820\text{ cm}^{-1}$ ). (Carbonyl is an attached, double-bonded X-CO group; the wavelength depends on the attachment.) A very similar band has been seen in *ISO* spectra of embedded protostars (Keane et al. 2001) where it is attributed to formaldehyde ( $\text{H}_2\text{CO}$ ). The wavelength of the formaldehyde band (Perrin, Keller & Flaud 2003) is indicated by the vertical line in the figure. But other molecules can contain carbonyl groups and a precise identification is difficult to make.

#### 4.2.6 The 10- $\mu\text{m}$ band

An absorption feature at 10  $\mu\text{m}$  is seen in a few Galactic carbon stars (Volk, Xiong & Kwok 2000; Sloan et al. 1998; Pitman, Hofmeister & Speck 2006). Jørgensen et al. (2000) find it in TT Cyg, but not in two other carbon stars they study; their fig. 1 indicates it is also present in R Scl. The origin is disputed. Clément et al. (2005) fit this band using solid silicon nitrite particles,  $\text{Si}_3\text{N}_4$ . Speck, Barlow & Skinner (1997) and Volk et al. (2000) suggest interstellar silicate absorption; to fit the shape, additional SiC absorption is required. Jørgensen et al. (2000) identify the band instead with  $\text{C}_3$  (see their fig. 11). In their models, the band is only present at high C/O ratio.

In our sample, this band appears to be present in NGC 1978 IR4. The middle panel of Fig. 8 shows the continuum-subtracted spectrum. The location and width of the band is fairly well reproduced with  $\text{C}_3$  but there are differences in the shape. (The model profile is calculated: no laboratory measurements of the 10- $\mu\text{m}$   $\text{C}_3$  exist.) There is a possibility that this absorption feature is also present in other sources in our sample. However, the neighbouring SiC feature makes it difficult to associate a continuum, and its presence cannot be confirmed.

The presence of the band in an LMC star argues against the interstellar origin proposed by Speck et al. (1997), because the line-of-sight extinction to the LMC is too small to give significant silicate absorption. A contribution from SiC absorption, as required by the silicate hypothesis, is also ruled out: this would only be in absorption in dense, cool shells, while we see the 10- $\mu\text{m}$  absorption in a blue, unobscured star. The photospheric origin argues against an identification with silicon nitrite dust (Clément et al. 2005). The identification suggested by Jørgensen et al. (2000) fits our available constraints. We therefore favour  $\text{C}_3$  as the probable carrier.

#### 4.2.7 SiS

SiS has three bands at 6.6–6.7  $\mu\text{m}$  but the IRS resolution is not high enough to detect these;  $R = 2000$  would be required.

### 4.3 Band strengths

We define the strength of the molecular absorption bands through their equivalent widths, and quantify the dust emission bands by their integrated line-to-continuum ratio. We use the adjacent continuum to define a linear (sloping) continuum distribution across each band and define the equivalent width in the usual way. Table 3 lists the wavelengths used to estimate the continuum for the  $\text{C}_2\text{H}_2$  (7.5  $\mu\text{m}$ ), SiC (11.3  $\mu\text{m}$ ) and  $\text{C}_2\text{H}_2$  (13.7  $\mu\text{m}$ ).

For the 13.7- $\mu\text{m}$  band, the equivalent width mainly refers to the narrow component; the broad component extends beyond the chosen continuum wavelengths.

**Table 3.** Wavelengths used to estimate the continua for the SiC and  $\text{C}_2\text{H}_2$  spectral features.

Features	$\lambda$ ( $\mu\text{m}$ )	Blue continuum ( $\mu\text{m}$ )	Red continuum ( $\mu\text{m}$ )
$\text{C}_2\text{H}_2$	7.5	6.08–6.77	8.22–8.55
SiC	11.3	9.50–10.10	12.80–13.40
$\text{C}_2\text{H}_2$	13.7	12.80–13.40	14.10–14.70

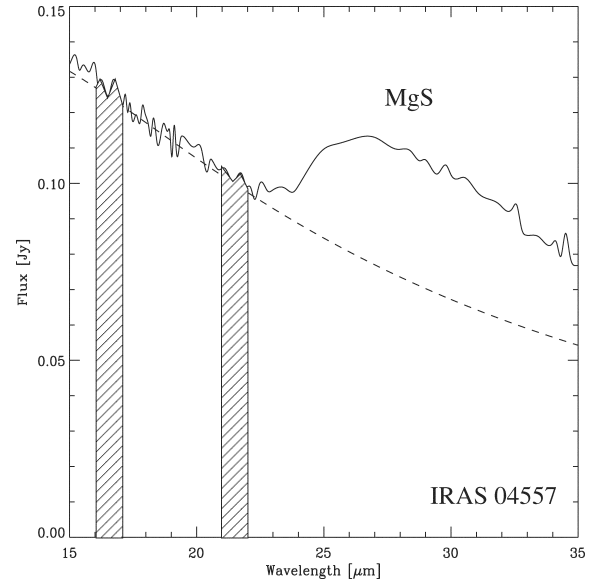


**Figure 9.** The continuum underlying the MgS feature is subtracted using a blackbody, whose temperature is defined using the [16.5]–[21.5] colour. The hatched bars display the wavelengths used to determine the [16.5] and [21.5] colours. The dashed line represents the blackbody fit to the spectrum of IRAS 04557–6753, as an example.

The continuum underneath the MgS band cannot be measured in this way, because the band extends beyond the red edge of the spectral coverage of the IRS. We instead use a blackbody to approximate the continuum, and give the strength as a line-to-continuum ratio integrated over the feature up to 38  $\mu\text{m}$ . This definition excludes the part of the emission feature not covered in the spectra. The blackbody is defined using the [16.5]–[21.5] colour discussed below (see Fig. 9). Table 4 lists the resulting values.

## 5 CONTINUUM COLOURS

### 5.1 The Manchester system

Much of the observed spectral range is covered by the molecular and dust bands discussed above. This leaves the continuum poorly defined: one needs to select specific wavelength regions which avoid these bands. The blue continuum is most affected by molecular bands; the red continuum is in many cases obliterated beyond 25  $\mu\text{m}$  by the 30- $\mu\text{m}$  MgS band.

We have selected four narrow regions which can be used for dusty carbon stars. The regions avoid most, but not all, of the obvious absorption and emission bands. Table 5 lists the continuum bands which define the Manchester system. Table 5 also lists the adopted zero-point for the bands. These are extrapolated from the standard bands, and aim to return a zero colour for a Rayleigh–Jeans tail.

**Table 4.** Strength of the molecular and dust features, in terms of either the equivalent width (EW) for molecular absorption bands, and the integrated line-to-continuum ratio (L/C) for the dust emission features. The central wavelength of the SiC band is also listed. The final column gives the continuum (blackbody) temperature, derived from the [16.5]–[21.5] colour listed in Table 6.

Target	EW (7.5 $\mu\text{m}$ )	EW (13.7 $\mu\text{m}$ )	L/C (SiC)	$\lambda_c$	L/C (MgS)	$T$ (K)
TRM 72	0.052 $\pm$ 0.005	0.068 $\pm$ 0.006	0.073 $\pm$ 0.002	11.37	0	1018
IRAS 04557	0.156 $\pm$ 0.004	0.066 $\pm$ 0.003	0.123 $\pm$ 0.003	11.30	0.412	426
IRAS 05009	0.069 $\pm$ 0.005	0.062 $\pm$ 0.004	0.159 $\pm$ 0.003	11.31	0.249	619
IRAS 05112	0.121 $\pm$ 0.005	0.066 $\pm$ 0.003	0.099 $\pm$ 0.002	11.34	0.271	396
IRAS 05113	0.133 $\pm$ 0.008	0.049 $\pm$ 0.004	0.094 $\pm$ 0.004	11.34	0.215	540
IRAS 05132	0.092 $\pm$ 0.006	0.071 $\pm$ 0.005	0.117 $\pm$ 0.004	11.27	0.198	557
IRAS 05190	0.135 $\pm$ 0.004	0.074 $\pm$ 0.004	0.104 $\pm$ 0.003	11.37	0.374	398
IRAS 05278	0.082 $\pm$ 0.004	0.075 $\pm$ 0.003	0.111 $\pm$ 0.003	11.32	0.407	421
GRRV 38	0.218 $\pm$ 0.023	0.118 $\pm$ 0.025	0.143 $\pm$ 0.019	11.14	0	858
IRAS 05295	0.092 $\pm$ 0.007	0.057 $\pm$ 0.004	0.086 $\pm$ 0.002	11.34	0.162	462
IRAS 05360	0.092 $\pm$ 0.004	0.051 $\pm$ 0.006	0.180 $\pm$ 0.006	11.19	0.624	395
MSX LMC 219	0.111 $\pm$ 0.005	0.061 $\pm$ 0.004	0.108 $\pm$ 0.003	11.29	0.336	393
MSX LMC 341	0.083 $\pm$ 0.007	0.063 $\pm$ 0.005	0.153 $\pm$ 0.004	11.16	0.637	482
MSX LMC 349	0.079 $\pm$ 0.007	0.049 $\pm$ 0.005	0.173 $\pm$ 0.004	11.18	0.713	470
MSX LMC 441	0.129 $\pm$ 0.007	0.056 $\pm$ 0.004	0.125 $\pm$ 0.003	11.26	0.446	427
MSX LMC 443	0.135 $\pm$ 0.008	0.054 $\pm$ 0.007	0.184 $\pm$ 0.006	11.18	0.459	467
MSX LMC 494	0.109 $\pm$ 0.007	0.039 $\pm$ 0.003	0.080 $\pm$ 0.003	11.31	0	780
MSX LMC 601	0.016 $\pm$ 0.005	0.060 $\pm$ 0.005	0.056 $\pm$ 0.003	11.30	0	703
MSX LMC 679	0.122 $\pm$ 0.006	0.044 $\pm$ 0.004	0.151 $\pm$ 0.004	11.22	0.477	415
MSX LMC 743	0.158 $\pm$ 0.005	0.042 $\pm$ 0.004	0.156 $\pm$ 0.004	11.24	0.383	455
MSX LMC 749	0.120 $\pm$ 0.003	0.076 $\pm$ 0.003	0.058 $\pm$ 0.004	11.25	0	865
MSX LMC 754	0.121 $\pm$ 0.006	0.053 $\pm$ 0.004	0.146 $\pm$ 0.006	11.32	0	726
MSX LMC 967	0.085 $\pm$ 0.003	0.058 $\pm$ 0.003	0.086 $\pm$ 0.003	11.30	0	742
NGC 1978 MIR1	0.157 $\pm$ 0.004	0.064 $\pm$ 0.006	0.162 $\pm$ 0.005	11.30	0.528	446
NGC 1978 IR1	0.123 $\pm$ 0.003	0.070 $\pm$ 0.004	0.094 $\pm$ 0.004	11.23	0	1179
NGC 1978 IR4	0.172 $\pm$ 0.010	0.082 $\pm$ 0.009	0.107 $\pm$ 0.006	11.50	0	>10 <sup>3</sup>
TRM 88	0.051 $\pm$ 0.006	0.064 $\pm$ 0.005	0.065 $\pm$ 0.004	11.26	0	684

**Table 5.** Mid-IR continuum bands for carbon stars for the so-called ‘Manchester system’. The last column gives the adopted flux density corresponding to zero magnitude.

Central $\lambda$ ( $\mu\text{m}$ )	$\lambda$ -range ( $\mu\text{m}$ )	$F_0$ (Jy)
6.4	6.25–6.55	96.5
9.3	9.1–9.5	45.7
16.5	16–17	15.4
21.5	21–22	9.1

The 6.4- $\mu\text{m}$  band is situated between the SiS bands at 6.6  $\mu\text{m}$  and CS at 7  $\mu\text{m}$  on the red side, and the CO/C<sub>3</sub> band at 5  $\mu\text{m}$  on the blue (Aoki et al. 1998). The wings of these molecular bands may still affect our chosen 6.4- $\mu\text{m}$  band. There is also overlap with the 6.2- $\mu\text{m}$  polycyclic aromatic hydrocarbon (PAH) feature, but this feature requires UV excitation and is seen in planetary nebulae and post-AGB stars but not spectra from AGB stars.

The 9.3- $\mu\text{m}$  band is blueward of the SiC dust band, and redward of the CS bands and C<sub>2</sub>H<sub>2</sub> bands at 7–8  $\mu\text{m}$  (Aoki et al. 1999). Bands from molecules such as NH<sub>3</sub> and C<sub>2</sub>H<sub>4</sub> may also depress the continuum by a few per cent (Cernicharo et al. 2001a). However, the 9.3- $\mu\text{m}$  band is situated in the possible C<sub>3</sub> band discussed above.

The two bands at 16.5 and 21.5  $\mu\text{m}$  do not overlap with any strong molecular or dust features in carbon-rich material; it is situated just redward of the broad P-branch 14- $\mu\text{m}$  C<sub>2</sub>H<sub>2</sub> band, which extends to 16  $\mu\text{m}$ . There is a weak hydrocarbon feature at the blue edge of the chosen band (Cernicharo et al. 2001b). The strong and still

unidentified 21- $\mu\text{m}$  dust feature is seen only in post-AGB stars. The chosen regions also avoid potential instrumental problems in the IRS, such as the LL1/LL2 interface.

The Manchester system can therefore be used to define the continuum within a few per cent, for carbon-rich AGB stars.

## 5.2 Manchester colours

Table 6 lists the continuum fluxes of all observed targets in the Manchester system. These are derived by integrating the IRS spectra over the bands. We give the colours using the zero-points of Table 5. Sloan et al. (2006b) give similar colours for SMC stars.

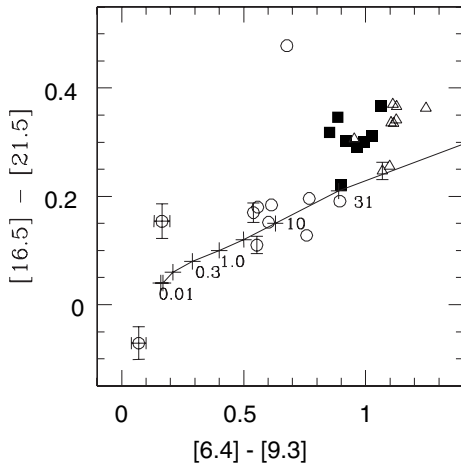
Table 6 lists a blackbody colour temperature derived from the [16.5]–[21.5] colour. For the bluest spectra, the values become poorly defined as the red colour approaches the Rayleigh–Jeans limit, but for the majority of objects a reasonable value is derived. Apart from NGC 1978 IR4 with photospheric colours, the colour temperatures range from  $\sim$ 1200 K for NGC 1978 IR1 to around 400 K for the coolest objects.

Fig. 10 shows the IRS colour–colour diagram based on the Manchester system for our targets. Error bars are indicated where the size of the bars exceeds the size of the symbol. The errors are calculated by comparing the spectra from the separate nod positions in each aperture, and do not include systematic effects such as calibration uncertainties or background subtraction. The majority of the stars fall on a well determined sequence. There are three exceptions: two stars are much bluer in [6.4]–[9.3], and one star is too red in [16.5]–[21.5] by approximately 0.25 mag.

The first two stars are GRRV 38 and NGC 1978 IR4. Both of these have spectral energy distributions largely consistent with naked

**Table 6.** Photometry: fluxes and colours using the narrow Manchester continuum bands for carbon stars. For the colours in the last two columns, we adopt the zero-points of Table 5. NGC 1978 IR4 was observed twice and both observations are listed.

Target	$F_{6.4}$ (Jy)	$F_{9.3}$ (Jy)	$F_{16.5}$ (Jy)	$F_{21.5}$ (Jy)	[6.4]–[9.3] (mag)	[16.5]–[21.5] (mag)
TRM 72	0.211 ± 0.001	0.201 ± 0.000	0.119 ± 0.001	0.079 ± 0.001	0.758 ± 0.005	0.128 ± 0.015
IRAS 04557	0.133 ± 0.001	0.174 ± 0.001	0.128 ± 0.001	0.102 ± 0.001	1.104 ± 0.010	0.336 ± 0.009
IRAS 05009	0.228 ± 0.001	0.247 ± 0.001	0.156 ± 0.001	0.112 ± 0.001	0.898 ± 0.005	0.220 ± 0.013
IRAS 05112	0.231 ± 0.002	0.309 ± 0.001	0.233 ± 0.001	0.192 ± 0.001	1.127 ± 0.008	0.336 ± 0.007
IRAS 05113	0.160 ± 0.001	0.209 ± 0.001	0.154 ± 0.001	0.115 ± 0.001	1.098 ± 0.008	0.256 ± 0.011
IRAS 05132	0.143 ± 0.001	0.181 ± 0.001	0.132 ± 0.001	0.098 ± 0.001	1.068 ± 0.008	0.247 ± 0.016
IRAS 05190	0.225 ± 0.002	0.336 ± 0.000	0.295 ± 0.001	0.242 ± 0.001	1.247 ± 0.010	0.363 ± 0.007
IRAS 05278	0.604 ± 0.003	0.807 ± 0.002	0.563 ± 0.004	0.454 ± 0.002	1.126 ± 0.006	0.341 ± 0.008
GRRV 38	0.067 ± 0.001	0.037 ± 0.001	0.021 ± 0.001	0.014 ± 0.000	0.165 ± 0.033	0.154 ± 0.032
IRAS 05295	0.150 ± 0.001	0.171 ± 0.000	0.115 ± 0.001	0.090 ± 0.001	0.953 ± 0.006	0.306 ± 0.009
IRAS 05360	0.107 ± 0.001	0.135 ± 0.001	0.089 ± 0.001	0.074 ± 0.001	1.062 ± 0.006	0.367 ± 0.014
MSX LMC 219	0.112 ± 0.001	0.148 ± 0.001	0.097 ± 0.000	0.080 ± 0.001	1.112 ± 0.009	0.370 ± 0.009
MSX LMC 341	0.109 ± 0.000	0.126 ± 0.001	0.078 ± 0.001	0.060 ± 0.000	0.963 ± 0.006	0.291 ± 0.012
MSX LMC 349	0.141 ± 0.001	0.166 ± 0.000	0.103 ± 0.001	0.080 ± 0.001	0.994 ± 0.007	0.300 ± 0.009
MSX LMC 441	0.137 ± 0.001	0.181 ± 0.001	0.119 ± 0.001	0.096 ± 0.000	1.115 ± 0.013	0.335 ± 0.008
MSX LMC 443	0.083 ± 0.001	0.092 ± 0.000	0.055 ± 0.000	0.042 ± 0.000	0.918 ± 0.008	0.302 ± 0.014
MSX LMC 494	0.094 ± 0.000	0.073 ± 0.000	0.035 ± 0.000	0.024 ± 0.000	0.540 ± 0.006	0.170 ± 0.018
MSX LMC 601	0.115 ± 0.001	0.124 ± 0.000	0.074 ± 0.000	0.052 ± 0.001	0.894 ± 0.006	0.191 ± 0.012
MSX LMC 663	0.116 ± 0.001	0.102 ± 0.000	0.078 ± 0.000	0.072 ± 0.000	0.677 ± 0.006	0.478 ± 0.007
MSX LMC 679	0.135 ± 0.001	0.144 ± 0.000	0.085 ± 0.001	0.069 ± 0.000	0.886 ± 0.006	0.346 ± 0.010
MSX LMC 743	0.093 ± 0.000	0.113 ± 0.000	0.067 ± 0.000	0.053 ± 0.000	1.026 ± 0.006	0.311 ± 0.009
MSX LMC 749	0.238 ± 0.001	0.196 ± 0.000	0.101 ± 0.000	0.068 ± 0.001	0.602 ± 0.003	0.152 ± 0.011
MSX LMC 754	0.086 ± 0.000	0.072 ± 0.000	0.033 ± 0.000	0.023 ± 0.000	0.614 ± 0.009	0.184 ± 0.014
MSX LMC 967	0.182 ± 0.000	0.144 ± 0.001	0.074 ± 0.001	0.051 ± 0.000	0.558 ± 0.005	0.180 ± 0.011
NGC 1978 MIR1	0.112 ± 0.001	0.116 ± 0.000	0.072 ± 0.001	0.057 ± 0.000	0.852 ± 0.006	0.318 ± 0.009
NGC 1978 IR4	0.042 ± 0.000	0.021 ± 0.000	0.012 ± 0.000	0.007 ± 0.000	0.079 ± 0.024	0.008 ± 0.031
NGC 1978 IR4	0.045 ± 0.001	0.022 ± 0.000	0.012 ± 0.000	0.006 ± 0.000	0.061 ± 0.025	−0.134 ± 0.026
NGC 1978 IR1	0.106 ± 0.000	0.084 ± 0.001	0.039 ± 0.000	0.025 ± 0.000	0.554 ± 0.007	0.110 ± 0.016
TRM 88	0.098 ± 0.001	0.094 ± 0.001	0.052 ± 0.001	0.037 ± 0.000	0.769 ± 0.009	0.196 ± 0.013



**Figure 10.** The [6.4]–[9.3] versus [16.5]–[21.5] colour–colour diagram. Symbols are defined in Fig. 2. (Open triangles are used here for reasons of clarity.) The drawn line represents a series of DUSTY models; the optical depth at 1  $\mu\text{m}$  of the models is indicated.

carbon stars. They are also faint in the IRS wavelength range and the colours have larger uncertainties than for the other stars, but the error bars shown on the figure indicate that the flux uncertainties do not affect their positions in this diagram. The last star is MSX LMC 663, in which the 21.5- $\mu\text{m}$  band includes an additional emission component.

All other stars show continuum emission dominated by circumstellar dust over all wavelengths considered here. The good correlation between the two colours confirms the choice of the continuum regions.

We calculated a series of benchmark dust models, to compare to the colours. The models used the DUSTY code, with a density distribution of a radiation-driven wind (Elitzur & Ivezić 2001),  $\rho \sim r^{-1.8}$ . A single grain diameter of 0.1  $\mu\text{m}$  was used, with a condensation temperature of 10<sup>3</sup> K, which determines the inner radius of the shell. Models were run with an optical depth  $\tau$  at 1  $\mu\text{m}$  ranging from 0.01 to 100. For the central star we assumed a blackbody of  $T = 2800$  K. A dust mixture of 95 per cent amorphous carbon (Hanner 1988) and 5 per cent SiC (Pegourie 1988) was used. The resultant spectra were used to measure the flux through the bandpasses, converted to colours using the zero-points of Table 5. Such models lack the important molecular bands needed to fit the detail of the observed spectra: this will be the subject of a forthcoming paper. The drawn line in Fig. 10 shows the models. The optical depth at 1  $\mu\text{m}$  is listed along the curve; locations are indicated by plus signs. The models show considerable optical depth for almost all objects.

At  $\tau = 0.01$ , the mass-loss rate is  $\dot{M} = 8 \times 10^{-8} M_{\odot} \text{yr}^{-1}$  for  $L = 10^4 L_{\odot}$  and LMC metallicity. GRRV 38 and NGC 1978 IR4 have mass-loss rates close to this value. All other stars have  $\dot{M} \gtrsim 10^{-5} M_{\odot} \text{yr}^{-1}$  (e.g. van Loon et al. 2006). GRRV 38 and NGC 1978 IR4 have mass-loss rates close to the nuclear burning rate (van Loon et al. 1999a). According to the definition given in Section 1, all other stars in our sample are in the superwind phase.

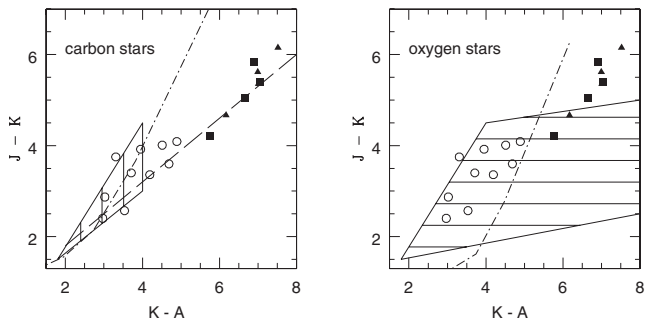


**Figure 11.** Source classification diagram based on Egan et al. (2001). The hashed area in the left-hand panel indicates the colour range of model carbon stars, taken from the SKY model of Wainscoat et al. (1992). The hashed region in the right-hand panel shows the same for oxygen-rich stars. The symbols are our carbon star sample, with symbols as defined in Fig. 2. The dashed line in the left-hand panel indicates the observed locus of obscured carbon stars. The dash-dotted line shows the colour sequence for oxygen-rich stars (right-hand panel) and carbon-rich (left-hand panel) DUSTY models.

## 6 DISCUSSION

### 6.1 Colour selection of carbon stars

Almost all sources presented here are carbon stars. Only two oxygen-rich objects were found in our entire sample of LMC stars, and only one of these is classified as an AGB star.

The colour criterion to separate oxygen-rich and carbon-rich stars, suggested by Egan et al. (2001), is based on the  $J - K$  versus  $K - A$  colours. Fig. 11 shows the diagram. Based on these colours, a higher fraction of oxygen-rich dust shells would have been expected. The hashed regions indicate the colour range shown by their model carbon stars (left-hand panel) and oxygen stars (right-hand panel), based on the SKY model of Wainscoat et al. (1992). Overplotted are the location of the stars in our sample. These mostly have colours redder than shown by any of the model carbon stars included in the SKY model. The distribution of our stars suggests that the SKY model can be extrapolated to redder stars. For obscured stars, there is considerable overlap in continuum colours between oxygen-rich and carbon-rich stars. The carbon-rich models of Section 5.2 are indicated by the dot-dashed line in the right-hand panel: they do not reproduce the colours particularly well, possibly because they lack the important molecular bands. A line through the observed data points shows the true locations of carbon stars.

A breakdown of the Egan et al. (2001) classification scheme is to be expected due to the silicate feature. At low mass-loss rates, the silicate feature is strongly in emission. At higher mass-loss rates, this feature becomes a strong absorption feature. van Loon et al. (1997) show that at a particular  $J - K$ , oxygen-rich stars with low mass-loss rates are redder in  $K - [12]$  than carbon stars, whilst for high mass-loss rates the opposite is true. Inevitably, there is a range where classification is not possible using these colours. The MSX A band (6.8–10.8  $\mu\text{m}$ ) also contains part of the silicate feature, although less than the IRAS 12- $\mu\text{m}$  band. We calculated similar models as in Section 5.2, but for oxygen-rich dust. The stellar temperature was taken as 3200 K, and an Ossenkopf, Henning & Mathis (1992) warm ‘circumstellar’ silicate model was assumed. The dot-dashed line in the right-hand panel of Fig. 11 show the resulting track with optical depth. It does indeed traverse the region used by Egan et al. (2001) but the  $K - A$  colour reaches an effective limit whilst the  $J - K$  colour continues to redden. The accuracy of this track is limited.

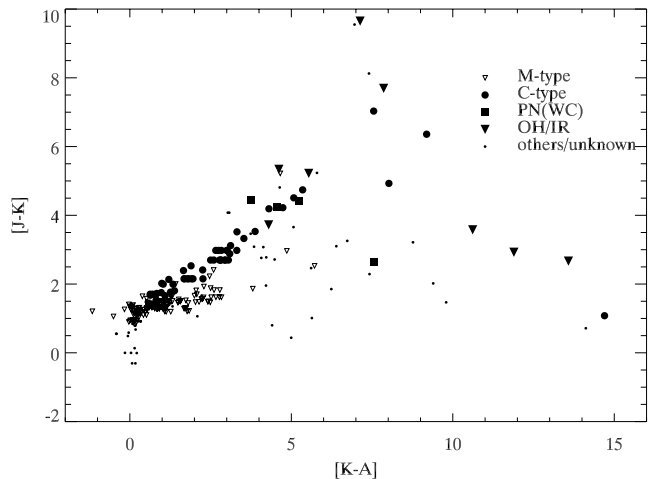


**Figure 12.** The  $J - K$  versus  $K - A$  diagram for evolved stars observed by *ISO*.

We used *ISO/SWS* and 2MASS data of Galactic stars to further examine the usefulness of nature of the  $J - K$  versus  $K - A$  diagram. The 271 *ISO/SWS* spectra (Kraemer et al. 2002) are convolved with the MSX A-band filter transmission curve. The zero magnitude for MSX is taken from Cohen, Hammersley & Egan (2000). The *ISO/SWS* stars are cross-correlated with the 2MASS data base and SIMBAD for identifications. Selection criteria are  $50 \text{ Jy} < F(A) < 10^4 \text{ Jy}$  for *ISO/SWS*, and 2MASS flags either a, b, c, d in all of the *JHK* bands. Some stars were observed several times and all of the A-band magnitudes were analysed individually. Spectral types range from B-type to M- and C-types, and post-AGB stars and planetary nebulae (PNe; all of them are WC), as well as young stellar objects are included. The M-type stars do not include dwarfs or subdwarfs. Fig. 12 shows the  $J - K$  versus  $K - A$  diagram for this Galactic sample. C-type refers to spectroscopically known carbon stars; these form a relatively narrow sequence. The isolated carbon star at  $K - A \sim 15$  is AFGL 5625: it shows a featureless spectrum (i.e. no SiC), except for 14- $\mu\text{m}$   $\text{C}_2\text{H}_2$ . The warmer M stars with  $J - K < 3$  also form a relatively narrow sequence, but the OH/IR stars show a large range of colours; OH/IR stars with  $K - A \sim 4-10$  show silicate emission with self-absorption on top (e.g. AFGL 2199, WX Psc), whilst OH/IR stars with  $K - A > 10$  show silicate absorption.

The separation between C-type and M-type stars with low mass-loss rates ( $2 < K - A < 3$ ) is due to photospheric, near-IR molecular bands. For oxygen-rich Mira stars, the  $K_s$ -flux is suppressed by water absorption (e.g. Matsuura et al. 2002b; Tej et al. 2003). For carbon stars, the  $J$ -band flux is suppressed by  $\text{C}_2$  and CN absorption (Loidl, Lançon & Jørgensen 2001). At high mass-loss rates, the carbon stars have well-defined colours which overlap with the (more scattered) oxygen-rich stars. Extremely red stars have no counterpart in the LMC sample of Egan et al. (2001), probably reflecting the 2MASS detection limit.

At high mass-loss rates, the Egan et al. (2001) diagram cannot distinguish carbon and oxygen-rich stars on an individual basis. However, stars on the carbon star sequence are statistically more likely to be carbon stars. Our selected stars fall on this sequence. At low mass-loss rates the colours of our targets are consistent with a carbon-rich nature. The sole oxygen-rich AGB star, IRAS 05003–6712, has colours consistent with the carbon-rich sequence ( $J - K = 2.95$ ,  $K - A = 3.8$ ), but at the blue end of the range where the two types overlap.

## 6.2 Molecules

All molecules suggested to be present (CO, C<sub>3</sub>, HCN, C<sub>2</sub>H<sub>2</sub>) are so-called parent molecules, which form in the photosphere and are found throughout the outflow, up to the photodissociation region at  $\approx 1\text{--}3 \times 10^{16}$  cm (Millar & Herbst 1994; Millar, Flores & Markwick 2001). C<sub>2</sub>H<sub>2</sub> is especially fundamental in the chemistry leading to large organic molecules such as PAHs. The abundance of these molecules is an important parameter for our understanding of chemistry in low-metallicity shells. van Loon et al. (1999b) noticed that the 3.1- $\mu$ m band in LMC stars was of the same strength as in Galactic stars, and suggested that the lower metallicity was compensated for by a higher C/O ratio. Matsuura et al. (2002a, 2005) find that C<sub>2</sub>H<sub>2</sub> is more abundant in LMC and SMC stars than in Galactic comparison stars, based on the 3.1 and 3.8- $\mu$ m absorption bands. Chemical models (Matsuura et al. 2002a) confirm the sensitivity of C<sub>2</sub>H<sub>2</sub> to the C/O ratio. The carbon enhancement from the third dredge-up leads to a higher C/O ratio for lower initial oxygen abundance. van Loon et al. (2006) find that HCN is weak compared to C<sub>2</sub>H<sub>2</sub> and that CS is absent, using the shape and structure in the 3.8- $\mu$ m absorption. They also show that the bands become sharper for stars with stronger pulsation, and they interpret this as evidence for cold molecular gas at some distance above the stellar photosphere.

Table 4 lists the equivalent widths of the molecular bands. Fig. 13 plots these values for the C<sub>2</sub>H<sub>2</sub> bands at 7.5  $\mu$ m and 13.7  $\mu$ m as a function of the [6.4]–[9.3] colour. The squares in the panels indicate the LMC stars. The 13.7- $\mu$ m band shows an especially narrow range in equivalent width. The 7.5- $\mu$ m band shows a large range, but neither correlates well with IR colour. The two ‘naked’ carbon stars show stronger bands. The equivalent width of the 13.7- $\mu$ m band refers only to the narrow component, as measured against the ‘continuum’ of the broad-band.

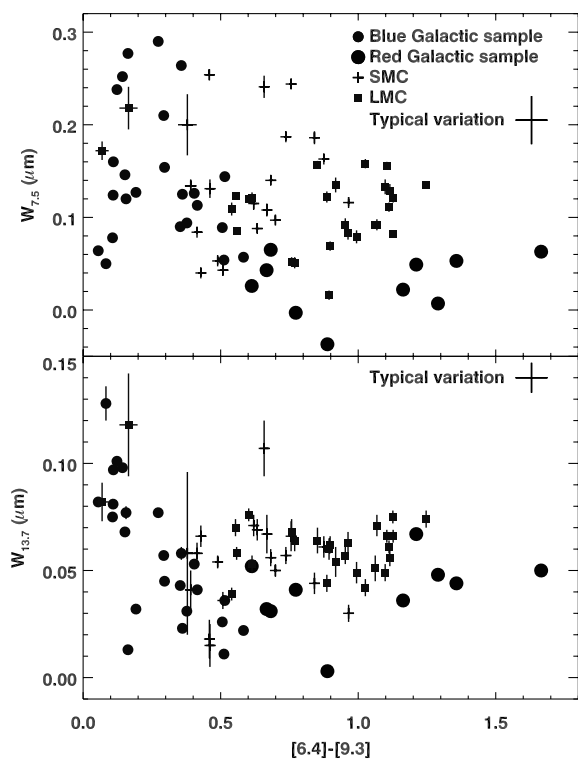


**Figure 13.** The strength of the C<sub>2</sub>H<sub>2</sub> features (7.5 and 13.7  $\mu$ m), as function of the [6.4]–[9.3] colour.

Sloan et al. (2006b) compare the strengths of these features for Galactic carbon stars and SMC carbon stars. They find that for stars with [6.4]–[9.3] > 0.6, the C<sub>2</sub>H<sub>2</sub> bands are stronger in the SMC than in the Galaxy, the difference being more readily apparent at 7.5  $\mu$ m than at 13.7  $\mu$ m. The difference of strength between Galactic, LMC and SMC stars is interpreted as due to higher abundances of C<sub>2</sub>H<sub>2</sub> in the SMC, in accordance with the prediction of Matsuura et al. (2005). Fig. 13 includes the Galactic and SMC samples. The equivalent widths are measured in the same way for all stars. The Galactic sample (based on *ISO* spectra) is divided into ‘blue’ and ‘red’ stars; blue colours are indicative of naked carbon stars.

The Galactic sample has a large range of [6.4]–[9.3] colour. The SMC sample in contrast shows a very limited colour range. For the same mass-loss rate one may expect lower metallicity stars to have lower optical depths because of a lower dust abundance. The SMC stars should show a lower [6.4]–[9.3] than the LMC stars, whilst the Galactic stars should show the reddest colours. This effect is best seen for [6.4]–[9.3] > 0.9. In the models of Section 5.2, an increase of a factor of 3 in optical depth reddens the [6.4]–[9.3] most at higher optical depth. The metallicity effect on colour is therefore much stronger for the redder stars, consistent with the distribution in the figure. The shift in colour with optical depth suggests the Galactic stars with [6.4]–[9.3] > 1.2 should be compared with the LMC stars around 0.9, and the SMC stars around 0.6. In the top panel, applying this shift shows a significant relation, with the 7.5- $\mu$ m feature becoming much stronger for lower metallicity. For the bluer mass-losing stars, where there is little change of colour with optical depth, the LMC stars have a stronger 7.5- $\mu$ m band than Galactic stars, but there is no clear offset between LMC and SMC stars.

Overall, these trends provide some evidence for the suggestion that the C<sub>2</sub>H<sub>2</sub> bands are stronger in lower metallicity environments. For the 13.7- $\mu$ m band, a small shift is also seen between the Galactic and the LMC stars, although less convincing than at 7.5  $\mu$ m, but the LMC and SMC stars show comparable equivalent widths.

The relatively small range in equivalent width of the C<sub>2</sub>H<sub>2</sub> band, for a large range of colour temperatures, can be explained if the molecule is located throughout the shell. It argues against an inner (warmer) molecular absorption region, filled in by dust emission originating further out, as proposed by (Jørgensen et al. 2000). However, there are complications in invoking molecular absorption over a wide range of radii, including the strong effect of density and temperature on the line strength, making it difficult to draw strong conclusions.

## 6.3 Dust

### 6.3.1 Temperature dependence

The *Spitzer* spectra show that SiC dust features are observed for most carbon stars, but the MgS feature is present in only a subset. The occurrence and strength of the two features is plotted for the LMC stars in Fig. 14, as a function of the continuum temperature (derived from [16.5]–[21.5]) and of the [6.4]–[9.3] colour, as a tracer of optical depth. The sources are put in three different groups: the circles indicate stars without an MgS feature; triangles (both open or filled) are used in different figures, indicating the same group of stars) show stars with MgS and weak SiC (defined as a line-to-continuum ratio less than 0.14); squares show stars with MgS and stronger SiC.

The presence of MgS correlates strongly with the dust temperature. There is a sharp division at a (blackbody) temperature of

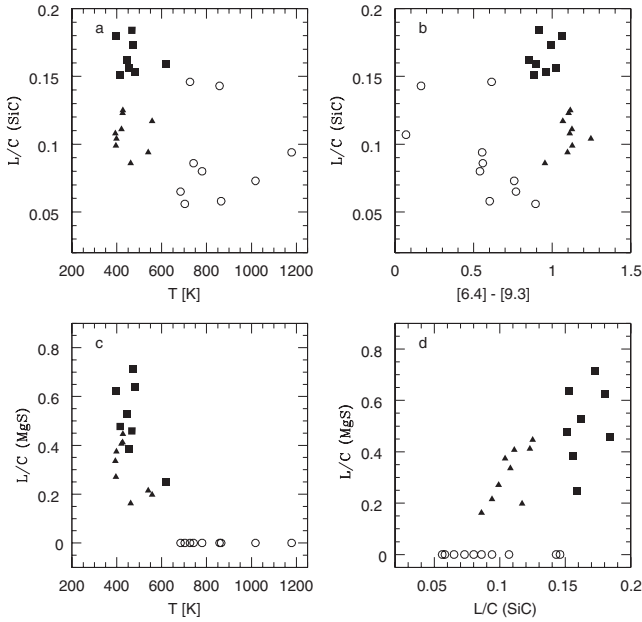


**Figure 14.** The strength of the 11- $\mu$ m SiC and the 30- $\mu$ m MgS bands, as a function of the dust continuum temperature (derived from [16.5]–[21.5]), and the [6.4]–[9.3] colour. Circles: stars without an MgS feature; squares: stars with an MgS feature and a strong SiC feature; triangles: stars with an MgS feature and a weak SiC feature.

$T = 650$  K: none of the stars with hotter dust show MgS, whilst all stars with cooler dust do. Between dust temperatures of 500 and 600 K the MgS feature is relatively weak. (The MgS feature is seen in general for stars with periods (Table 2) longer than 650 d.) In contrast, SiC tends to be weaker at high dust temperatures but is almost always present. The difference can be understood in terms of the formation mechanism of the different dust species. Solid SiC condenses directly from the gas at high temperatures. MgS grows as a surface on pre-existing grains (Nuth et al. 1985); this process only starts at temperatures around 600 K and is complete around 300 K.

### 6.3.2 Metallicity dependence

Fig. 15 compares the strengths of the SiC and MgS features. Sloan et al. (2006b) find that the SiC and MgS features are weaker in the SMC than in the Galaxy. This is expected, as Mg, Si and S are not produced in AGB stars and their abundance should scale directly with metallicity. Our data show a more complicated picture, however.

The line-to-continuum ratios are plotted against [6.4]–[9.3]. As before, for the higher mass-loss stars the optical depth is less in the SMC, while at low optical depth SMC, LMC and Galactic stars can be compared at the same value for [6.4]–[9.3]. The top panel shows that at low optical depth ([6.4]–[9.3]  $\approx 0.5$ ), there is a clear sequence with the SiC line-to-continuum ratio diminishing with decreasing metallicity. At higher optical depth, the three samples indicate very similar ratios. Stars with ‘naked carbon star’ colours show a high line-to-continuum ratio, related to the weakness of the continuum, with a sequence clearly offset from the dusty stars. It is possible that here the continuum used to measure the feature strength is affected by molecular absorption bands, giving an artificially enhanced feature. The SiC features is flanked by two photospheric bands, attributed to  $C_2H_2$  and  $C_3$ , and a true continuum cannot easily be defined.

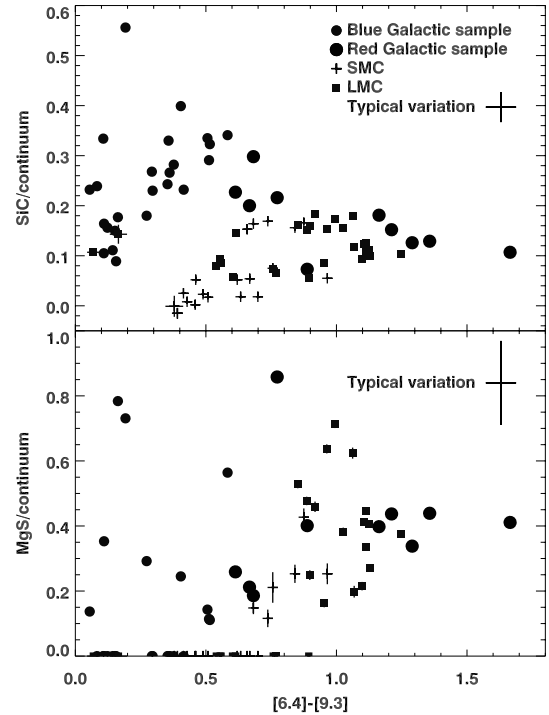


**Figure 15.** The strength of the SiC and MgS features as a function of the [6.4]–[9.3] colour.

The bottom panel of Fig. 15 illustrates the MgS feature. There is an indication that it is weaker in the SMC than in comparable Galactic and LMC stars. The LMC stars show a very large scatter and it is not possible to draw conclusions regarding its typical strength. We note that the continuum underneath the feature is not well defined in *Spitzer* spectra because of its long-wavelength cut-off.

In both cases the line-to-continuum ratio in dusty stars compares the feature strength with the underlying dust continuum, assumed to be due to amorphous carbon. As the carbon is dredged up in the star while the mineral constituents are not, the ratio is expected to decrease with decreasing metallicity. The SMC data clearly indicate that the emissivity ratio between minerals and amorphous carbon dust is lower at low metallicity, but the LMC data is inconclusive on this point.

The abundance of SiC is limited by the enriched carbon and the unenriched silicon. The abundance of MgS is limited by two unenriched elements. If the condensation is 100 per cent efficient, both will be affected similarly by metallicity. If the condensation operates at lower efficiency, the collision rate limits the dust formation, and the abundance of MgS would more strongly depend on metallicity than SiC ( $[MgS] \propto Z^2$ , while  $[SiC] \propto Z$ , where  $Z$  is the fractional abundance of metals). (Temperature effects may also contribute, as lower opacity leads to higher dust temperatures.) The spectra presented here do not support such a strong dependence on metallicity, but favour a linear relation. This supports a high condensation efficiency for MgS. Confirmation will require detailed modelling of the dust spectra.

### 6.3.3 Central wavelengths

The central wavelengths of the dust features are important diagnostics of the dust environment (Hony et al. 2002; Speck et al. 2005). We define the central wavelength (hereafter  $\lambda_{SiC}$ ) as the wavelength

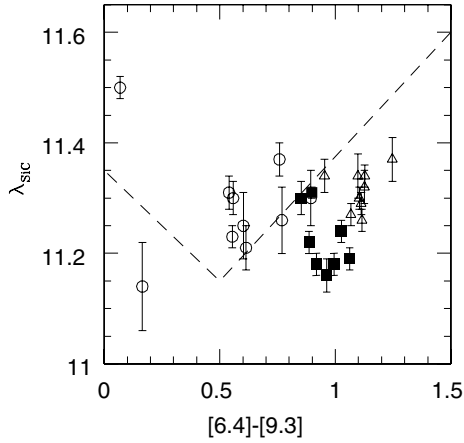


**Figure 16.** Apparent central wavelength of the SiC feature as a function of the [6.4]–[9.3] colour. The dashed line represents the distributions of Galactic carbon stars, according to Sloan et al. (2006b). Symbols are as in Fig. 14. (Open triangles are used for reasons of clarity.)

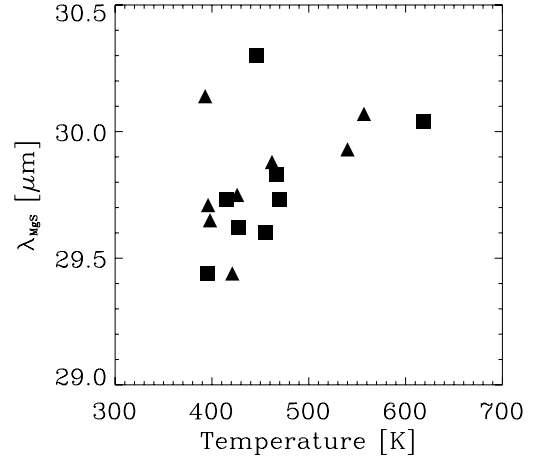
which bisects the flux distribution in the feature: i.e. after continuum subtraction, half the flux arises redward and half blueward. This definition is more stable against noise on the spectral energy distribution than the wavelength of peak emission strength. However, for MgS only part of the feature is covered by the *Spitzer* spectra and the derived central wavelength reflects this limit.

Fig. 16 shows  $\lambda_{\text{SiC}}$ , as a function of the [6.4]–[9.3] colour. Sloan et al. (2006b) find that for Galactic carbon stars with [6.4]–[9.3] > 0.5,  $\lambda_{\text{SiC}}$  increases monotonically with [6.4]–[9.3] colour, from  $\sim 11.20 \mu\text{m}$  up to  $\sim 11.70 \mu\text{m}$ . For bluer colours  $\lambda_{\text{SiC}}$  reddens again: their relation is indicated by the dashed line. In our LMC sample,  $\lambda_{\text{SiC}}$  is redder for the stars with weaker SiC features (triangles in Fig. 16). The LMC stars follow the slope of the relation of Sloan et al. (2006b), but offset towards redder [6.4]–[9.3].

We attribute the apparent reddening of the central wavelength with colour, for the redder stars, to the effect of the broad  $\text{C}_2\text{H}_2$  absorption. This band borders the SiC feature, and may overlap with it in wavelength. Our choice for red continuum falls by necessity within the broad-band. Stronger absorption in the R branch of the  $\text{C}_2\text{H}_2$  band will lead to a redder SiC wavelength as we measure it. Self-absorption of SiC can also introduce a wavelength shift (Speck et al. 2005). Extreme carbon stars with SiC absorption features occur in the Galaxy, but lack a counterpart in our sample. The shape of the SiC feature for the LMC stars shows little indication for absorption.

‘Naked’ carbon stars with [6.4]–[9.3] < 0.5 show a strong shift to longer wavelength of  $\lambda_{\text{SiC}}$ , with bluer colours. Here the explanation is not evident. It is however also possible that these stars have no SiC, but that 10 and 13  $\mu\text{m}$  absorption bands cause an artificial emission feature in between.

Fig. 17 shows the central wavelength of the MgS feature (hereafter  $\lambda_{\text{MgS}}$ ), as a function of the temperature derived from the [16.5]–[21.5] colour. Hony et al. (2002) show that the central wavelength of the MgS feature is independent of continuum temperatures. They explain this by the fact that MgS is partially heated by mid-IR radiation. In our sample, the MgS feature is observed only in stars spread over a small range of continuum temperatures. The suggestion of longer  $\lambda_{\text{MgS}}$  for higher dust temperatures is not conclusive. Our LMC sample shows  $\lambda_{\text{MgS}}$  similar to Galactic stars observed by Hony et al. (2002) within the same temperature range. Fig. 18 shows the shape of the continuum-subtracted MgS feature. There is no apparent correlation between the MgS feature shape and the



**Figure 17.** Apparent central wavelength of the MgS feature as a function of the temperature (derived from the [16.5]–[21.5] colour). Symbols are as in Fig. 14.

dust-continuum temperature. The short-wavelength band edge has a similar shape in all spectra. There is some separation between stars with relatively flat MgS band and stars where the band diminishes towards the red, but this separation does not show an evident correlation with dust temperature.

#### 6.3.4 Oxygen-rich dust

The current sample contains almost exclusively carbon-rich stars. Oxygen-rich mass-losing stars do exist in the LMC (e.g. Trams et al. 1999; Dijkstra et al. 2005). Comparing the  $J - K$  versus  $K - A$  diagram for MSX sources in Egan et al. (2001) with the diagrams in Section 6.1 shows that the majority of embedded LMC stars have colours consistent with the carbon star sequence, but some stars are bluer in  $K - A$  and these could be oxygen-rich.

Dust formation in oxygen-rich stars is dependent on metallicity-dependent minerals, such as corundum and various silicates. Oxygen-rich stars may therefore show reduced dust formation efficiency at low metallicity. For some stars, this could delay the superwind phase sufficiently to allow them to become a carbon star. Carbon stars are less affected by metallicity, as dust is produced from self-enriched carbon. It would be of interest to test whether oxygen-rich stars in the LMC stars show any evidence for a delayed or weaker superwind.

The predominance of mass-losing carbon stars implies that dust enrichment of the ISM at low metallicity by AGB stars will be strongly dominated by amorphous carbon dust, as compared to the Galaxy.

#### 6.4 Three groups

In Section 6.3.1, we have shown that the strength of the dust bands versus colours or temperatures permits us to identify three distinct group of carbon stars in our LMC sample. The three groups can be defined as (1) stars with a strong SiC feature and MgS, (2) stars with a weak SiC feature and MgS and (3) stars without an MgS feature.

Fig. 19 shows the spectral shapes of stars within those three groups, obtained by averaging the different spectra within each group. The shape of the SiC band is essentially identical between the first two groups, but the continuum on either side is different. The narrow 13.7- $\mu\text{m}$  band weakens as SiC becomes weaker, but

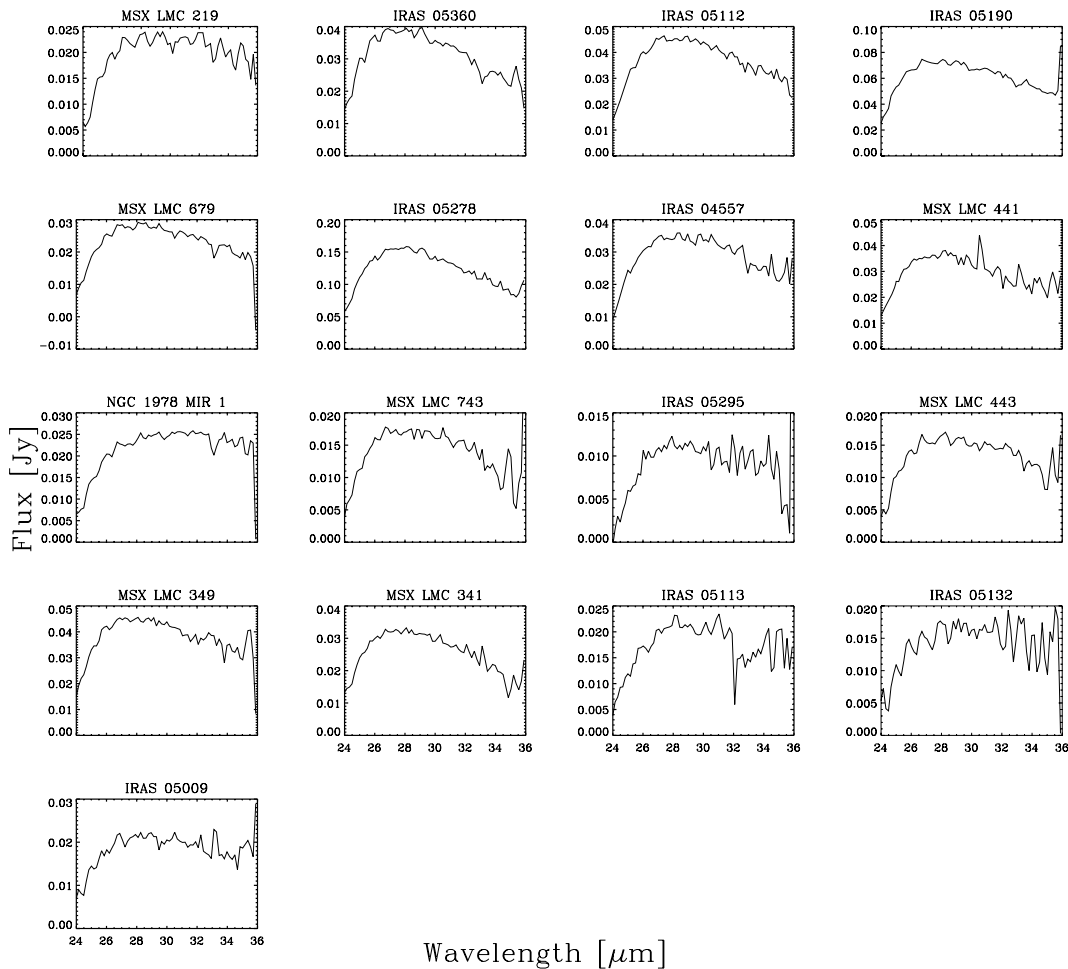


**Figure 18.** The continuum-subtracted shape of the MgS features observed in our LMC sample. The spectra are ordered by dust temperature, from blue spectra to red.

the broad-band between 12 and 16  $\mu\text{m}$  becomes much more prominent. This trend is best seen by comparing the slopes of the spectra. The blue slopes of the continua (5–9  $\mu\text{m}$ ) also show a difference between the three groups. This supports the explanation for the reddening with colour as due to the effect of continuum determination; we see no evidence for an SiC absorption component.

Such a classification can be compared with that proposed by Kraemer et al. (2002), who divide dusty carbon-rich stars into red (CR) and blue (CE). In our sample, about 10 stars would be classified as CE and the remainder (apart from the symbiotic C star) as CR. In the Galactic *ISO* sample of Kraemer et al. (2002), CE stars are somewhat more dominant. This difference is likely to be caused by selection effects, since our sample is selected based on mid-IR colours.

### 6.5 The final status of LMC AGB stars

In Section 2, we showed that we selected targets from the long sequence of increasingly red Magellanic Cloud AGB stars in the ( $K$ ,  $J - K$ ) diagram (Fig. 1). This sequence corresponds to increasing mass-loss rate and increasingly thick circumstellar shells. Most mid-IR point sources in the Magellanic Clouds lie on this sequence, although there are some more luminous exceptions (OH/IR stars). All but one of our targets turned out to be carbon-rich AGB stars (excluding the bright oxygen-rich star observed accidentally, and

the massive young stellar object). The one oxygen-rich AGB star is not particularly red ( $K$ ,  $J - K \sim 3$ ) and lies at the upper  $K$ -luminosity edge of the sequence. We also showed that the stars we have observed most likely have initial masses in the range  $\sim 1.5$ – $2.5 M_{\odot}$ .

The higher efficiency of the third dredge-up at low metallicity turns LIMS into carbon stars relatively early on the AGB. The stars at the beginning of the mass-loss sequence shown in Fig 1(a) are already optical carbon stars and it is expected that more evolved stars on the sequence would also be C stars. Such an expectation would only break down for massive and relatively rare AGB stars that lie above the sequence of Fig. 1(a) since such stars do not ever become carbon stars. Oxygen-rich mass-losing stars will most likely be stars with initial masses large than about  $4 M_{\odot}$ , where hot bottom burning prevents the star from becoming carbon-rich.

The picture that emerges from this is that, at LMC metallicity, all stars in the  $\sim 1.5$ – $2.5 M_{\odot}$  range are C stars by the time they develop substantial mass-loss rates and they remain C stars until their AGB evolution is terminated by the transition towards the planetary nebula phase of evolution. Although the most common AGB stars in the LMC will follow this behaviour, the more luminous and massive, but rare, OH/IR stars in the LMC (e.g. Wood et al. 1992; Marshall et al. 2004) can survive as oxygen-rich objects well into the dust-enshrouded superwind phase, perhaps even to the end of their AGB evolution.

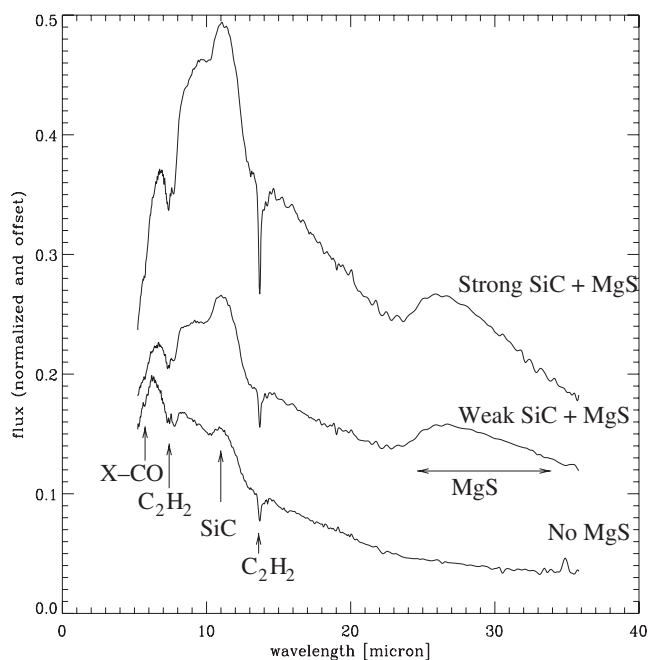


**Figure 19.** Spectra of the three object classes observed, the first class (top) containing objects displaying a SiC feature and a strong MgS feature, the second (middle) a SiC and a weak MgS feature, the last one (bottom) displaying no MgS feature. These three spectra are obtained by averaging the individual spectra for each class. Molecular and dust bands are indicated, including the carbonyl group.

## 7 CONCLUSIONS

We have presented a *Spitzer* survey of 29 mass-losing AGB stars in the LMC. All but two are classified as carbon stars, based on the IR spectra. One of the C stars is a symbiotic star. Two oxygen-rich stars were also present in the original survey: one was found to be a high-mass young stellar object (van Loon et al. 2005b). Bolometric magnitudes indicate that progenitor masses are mostly in the range 1.5–2.5  $M_{\odot}$ .

The spectra cover the wavelength range 5–38  $\mu\text{m}$ . The short-wavelength range, up to 16  $\mu\text{m}$ , is dominated by absorption bands caused by circumstellar and/or photospheric molecules. At the short edge, bands of CO and  $\text{C}_3$  cause a sharp drop of the stellar energy distribution towards the blue end of the spectral range. Absorption bands at 7.5 and 13.7  $\mu\text{m}$  are due to acetylene,  $\text{C}_2\text{H}_2$ . The 13.7- $\mu\text{m}$  band contains both a narrow and a broad component, the latter tracing hotter gas. These bands are also seen in two naked carbon stars in our sample.

Dust emission bands are present in our sample at 11 and at 30  $\mu\text{m}$ , due, respectively, to SiC and MgS. The first band is present in almost every object, regardless of dust temperature. MgS is only present when the dust temperature is below 650 K, in approximately half the sample. This is consistent with how these minerals form: SiC condenses directly out of the gas phase, but MgS is deposited on existing dust grains below a critical temperature.

We find a broad 10- $\mu\text{m}$  absorption band in our most naked carbon star. This band is known from Galactic carbon stars: it has previously been attributed to interstellar silicates, but this assignment can be ruled out for the LMC star. A recent assignment to silicon nitride particles can also be ruled out for emission at photospheric temperatures. This supports the identification with a  $\text{C}_3$  band, as proposed by Jørgensen et al. (2000).

A weak 5.8- $\mu\text{m}$  absorption feature, with a depth of a few per cent, seen in the average spectrum of our dusty carbon stars. The wavelength is consistent with a carbonyl group: a possible identification is with  $\text{H}_2\text{CO}$ .

Because of the many bands in the spectra, continuum definition is difficult. We define a set of four narrow bands, called the Manchester system, which can be used to trace the continuum for dusty carbon stars. The bands are centred at 6.4, 9.3, 16.5 and 21.5  $\mu\text{m}$ . The [6.4]–[9.3] colour is shown to be a measure of the optical depth in the shell. The [16.5]–[21.5] colour can be used to measure the dust temperature.

The classification scheme of mass-losing stars by Egan et al. (2001) is investigated. Based on this scheme, some stars in our sample were expected to be oxygen-rich. We show from current data, from dust models and from *ISO* spectra of Galactic stars, that for high mass-loss stars, the  $J - K$ ,  $K - A$  colours cannot easily distinguish oxygen-rich from carbon-rich stars. The fact that almost all our sample was found to be carbon-rich indicates that LMC stars in the mass range 1.5–2.5  $M_{\odot}$  become carbon stars before they develop thin dust shells.

The 7.5- $\mu\text{m}$   $\text{C}_2\text{H}_2$  band shows evidence for increasing equivalent width with decreasing metallicity. This trend is less clear for the 13.7- $\mu\text{m}$  band. The SiC band shows evidence for a much lower line-to-continuum ratio at the lowest metallicity (the SMC) but no strong difference between the LMC and the Galaxy. For MgS there is an indication for a sequence of decreasing line-to-continuum ratio with decreasing metallicity. We show that the central wavelength of the SiC feature depends on the [6.4]–[9.3] colour, consistent with Sloan et al. (2006b). This shift is however attributed to the continuum determination, affected by molecular absorption bands.

The increasing strength of the acetylene bands with decreasing metallicity can be explained by the effect of carbon dredge-up: a fixed amount of added carbon gives a higher C/O ratio at lower metallicity (less O), leaving more free carbon after the formation of CO. This free carbon may also explain the strong  $\text{C}_3$  in our spectra. SiC and MgS do not benefit from this effect, and their abundance is expected to scale more directly with metallicity.

We finally note that dust formation in oxygen-rich stars is dependent on metallicity-dependent minerals, such as corundum and various silicates. Oxygen-rich stars may therefore show relatively poor dust formation efficiency at low metallicity. Carbon stars, on the other hand, depend for dust on self-produced carbon and can form amorphous carbon efficiently. The earlier formation of carbon stars due to the third dredge-up, together with a possible difference in dust formation efficiency, means that dust enrichment of the ISM at low metallicity by AGB stars will be dominated by amorphous carbon dust, as compared to the Galaxy.

## ACKNOWLEDGMENTS

We appreciate the efforts of the IRS team at Cornell. AAZ, EL and MM acknowledge PPARC rolling grant support. PPARC also supported this research via a visitor grant. PAW acknowledges the support provided by a grant from the Australian Research Council. MM thanks the UMIST Peter Allen Travelling Grant. M. Cohen kindly provided us with the MSX filter transmission curve.

## REFERENCES

- Alves D. R., Rejkuba M., Minniti D., Cook K. H., 2002, *ApJ*, 573, L51  
 Aoki W., Tsuji T., Ohnaka K., 1998, *A&A*, 340, 222  
 Aoki W., Tsuji T., Ohnaka K., 1999, *A&A*, 350, 945

- Baron Y., Papoular R., Jourdain de Muizon M., Pegourie B., 1987, *A&A*, 186, 271
- Bica E. L. D., Schmitt H. R., Dutra C. M., Oliveira H. L., 1999, *AJ*, 117, 238
- Bloeker T., 1995, *A&A*, 297, 727
- Cami J., 2002, PhD thesis, Univ. Amsterdam
- Cernicharo J., Yamamura I., González-Alfonso E., de Jong T., Heras A., Escribano R., Ortigoso J., 1999, *ApJ*, 526, L41
- Cernicharo J., Heras A. M., Pardo J. R., Tielens A. G. G. M., Guélin M., Dartois E., Neri R., Waters L. B. F. M., 2001a, *ApJ*, 546, L127
- Cernicharo J., Heras A. M., Tielens A. G. G. M., Pardo J. R., Herpin F., Guélin M., Waters L. B. F. M., 2001b, *ApJ*, 546, L123
- Cioni M.-R. L., Marquette J.-B., Loup C., Azzopardi M., Habing H. J., Lasserre T., Lesquoy E., 2001, *A&A*, 377, 945
- Cioni M.-R. L. et al., 2003, *A&A*, 406, 51
- Clément D., Mutschke H., Klein R., Henning T., 2003, *ApJ*, 594, 642
- Clément D., Mutschke H., Klein R., Jäger C., Dorschner J., Sturm E., Henning T., 2005, *ApJ*, 621, 985
- Cohen M., Hammersley P. L., Egan M. P., 2000, *AJ*, 120, 3362
- Dijkstra C., Speck A. K., Reid R. B., Abraham P., 2005, *ApJ*, 633, L133
- Dray L. M., Tout C. A., Karakas A. I., Lattanzio J. C., 2003, *MNRAS*, 338, 973
- Dwek E., 1998, *ApJ*, 501, 643
- Edmunds M. G., 2001, *MNRAS*, 328, 223
- Egan M. P., Van Dyk S. D., Price S. D., 2001, *AJ*, 122, 1844
- Elitzur M., Ivezić Ž., 2001, *MNRAS*, 327, 403
- Feast M. W., Whitelock P. A., 1992, *MNRAS*, 259, 6
- Feast M. W., Glass I. S., Whitelock P. A., Catchpole R. M., 1989, *MNRAS*, 241, 375
- Feast M. W., Whitelock P. A., Marang F., 2003, *MNRAS*, 346, 878
- Forrest W. J., Houck J. R., McCarthy J. F., 1981, *ApJ*, 248, 195
- Gautschi-Loidl R., Höfner S., Jørgensen U. G., Hron J., 2004, *A&A*, 422, 289
- Gavilán M., Buell J. F., Mollá M., 2005, *A&A*, 432, 861
- Glass I. S., Reid N., 1985, *MNRAS*, 214, 405
- Goebel J. H., Moseley S. H., 1985, *ApJ*, 290, L35
- Goebel J. H., Bregman J. D., Witteborn F. C., Taylor B. J., Willner S. P., 1981, *ApJ*, 246, 455
- Goriely S., Mowlavi N., 2000, *A&A*, 362, 599
- Groenewegen M. A. T., 2004, *A&A*, 425, 595
- Hajduk M. et al., 2005, *Sci*, 308, 231
- Hanner M., 1988, Technical report, Grain Optical Properties
- Hony S., 2002, PhD thesis, Univ. Amsterdam
- Hony S., Bouwman J., 2004, *A&A*, 413, 981
- Hony S., Waters L. B. F. M., Tielens A. G. G. M., 2002, *A&A*, 390, 533
- Houck J. R. et al., 2004, *ApJS*, 154, 18
- Ita Y. et al., 2004, *MNRAS*, 353, 705
- Jørgensen U. G., Hron J., Loidl R., 2000, *A&A*, 356, 253
- Keane J. V., Tielens A. G. G. M., Boogert A. C. A., Schutte W. A., Whittet D. C. B., 2001, *A&A*, 376, 254
- Kemper F., Waters L. B. F. M., de Koter A., Tielens A. G. G. M., 2001, *A&A*, 369, 132
- Kraemer K. E., Sloan G. C., Price S. D., Walker H. J., 2002, *ApJS*, 140, 389
- Lah P., Kiss L. L., Bedding T. R., 2005, *MNRAS*, 359, L42
- Le Bertre T., 1992, *A&AS*, 94, 377
- Loidl R., Lançon A., Jørgensen U. G., 2001, *A&A*, 371, 1065
- Maeder A., 1992, *A&A*, 264, 105
- Marshall J. R., van Loon J. T., Matsuura M., Wood P. R., Zijlstra A. A., Whitelock P. A., 2004, *MNRAS*, 355, 1348
- Matsuura M., Zijlstra A. A., van Loon J. T., Yamamura I., Markwick A. J., Woods P. M., Waters L. B. F. M., 2002a, *ApJ*, 580, L133
- Matsuura M., Yamamura I., Cami J., Onaka T., Murakami H., 2002b, *A&A*, 383, 972
- Matsuura M. et al., 2005, *A&A*, 434, 691
- Millar T. J., Herbst E., 1994, *A&A*, 288, 561
- Millar T. J., Herbst E., Bettens R. P. A., 2000, *MNRAS*, 316, 195
- Millar T. J., Flores J. R., Markwick A. J., 2001, *MNRAS*, 327, 1173
- Molster F. J., Waters L. B. F. M., Tielens A. G. G. M., 2002, *A&A*, 382, 222
- Nishida S., Tanabé T., Nakada Y., Matsumoto S., Sekiguchi K., Glass I. S., 2000, *MNRAS*, 313, 136
- Nuth J. A., Moseley S. H., Silverberg R. F., Goebel J. H., Moore W. J., 1985, *ApJ*, 290, L41
- Ortiz R. et al., 2002, *A&A*, 388, 279
- Ossenkopf V., Henning T., Mathis J. S., 1992, *A&A*, 261, 567
- Papoular R., Cauchetier M., Begin S., Lecaer G., 1998, *A&A*, 329, 1035
- Pegourie B., 1988, *A&A*, 194, 335
- Perrin A., Keller F., Flaud J.-M., 2003, *J. Mol. Spectrosc.*, 221, 192
- Pitman K., Hofmeister A., Speck A., 2006, *MNRAS*, submitted
- Reid N., 1991, *ApJ*, 382, 143
- Reid N., Tinney C., Mould J., 1990, *ApJ*, 348, 98
- Romano D., Matteucci F., Ventura P., D'Antona F., 2001, *A&A*, 374, 646
- Sandin C., Höfner S., 2003, *A&A*, 398, 253
- Sloan G. C., Little-Marenin I. R., Price S. D., 1998, *AJ*, 115, 809
- Sloan G. C., Nerenberg P. S., Russell M. R., 2003, IRS Technical Report 03001
- Sloan G. C., Devost D., Bernard-Salas J., Wood P. R., Houck J. R., 2006a, *ApJ*, 638, 472
- Sloan G. C., Kraemer K. E., Matsuura M., Price S. D., Wood P. R., Egan M. P., 2006b, *ApJ*, in press
- Speck A. K., Barlow M. J., Skinner C. J., 1997, *MNRAS*, 288, 431
- Speck A. K., Thompson G. D., Hofmeister A. M., 2005, *ApJ*, 634, 426
- Tanabé T. et al., 1997, *Nat*, 385, 509
- Tej A., Lançon A., Scholz M., Wood P. R., 2003, *A&A*, 412, 481
- Trams N. R. et al., 1999, *A&A*, 346, 843
- Travaglio C., Randich S., Galli D., Lattanzio J., Elliott L. M., Forestini M., Ferrini F., 2001, *ApJ*, 559, 909
- Treffers R., Cohen M., 1974, *ApJ*, 188, 545
- Tsuji T., 1984, *A&A*, 134, 24
- van Loon J. T., Zijlstra A. A., Whitelock P. A., Waters L. B. F. M., Loup C., Trams N. R., 1997, *A&A*, 325, 585
- van Loon J. T., Groenewegen M. A. T., de Koter A., Trams N. R., Waters L. B. F. M., Zijlstra A. A., Whitelock P. A., Loup C., 1999a, *A&A*, 351, 559
- van Loon J. T., Zijlstra A. A., Groenewegen M. A. T., 1999b, *A&A*, 346, 805
- van Loon J. T., Marshall J. R., Zijlstra A. A., 2005a, *A&A*, 442, 597
- van Loon J. T. et al., 2005b, *MNRAS*, 364, L71
- van Loon J. T., Marshall J. R., Matsuura M., Zijlstra A. A., Wood P. R., Cohen M., Yamamura I., 2006, *A&A*, 447, 971
- Vassiliadis E., Wood P. R., 1993, *ApJ*, 413, 641
- Volk K., Xiong G., Kwok S., 2000, *ApJ*, 530, 408
- Volk K., Kwok S., Hrivnak B. J., Szczerba R., 2002, *ApJ*, 567, 412
- Wainscoat R. J., Cohen M., Volk K., Walker H. J., Schwartz D. E., 1992, *ApJS*, 83, 111
- Wanajo S., Nomoto K., Iwamoto N., Ishimaru Y., Beers T. C., 2006, *ApJ*, 636, 842
- Werner M. W. et al., 2004, *ApJS*, 154, 1
- Whitelock P. A., Feast M. W., van Loon J. T., Zijlstra A. A., 2003, *MNRAS*, 342, 86
- Will J.-M., Bomans D. J., Tucholke H.-J., de Boer K. S., Grebel E. K., Richtler T., Seggewiss W., Vallenari A., 1995, *A&AS*, 112, 367
- Willacy K., Millar T. J., 1997, *A&A*, 324, 237
- Willems F. J., 1988, *A&A*, 203, 51
- Willson L. A., 2000, *ARA&A*, 38, 573
- Wood P. R., 1998, *A&A*, 338, 592
- Wood P. R., Bessell M. S., Fox M. W., 1983, *ApJ*, 272, 99
- Wood P. R., Whiteoak J. B., Hughes S. M. G., Bessell M. S., Gardner F. F., Hyland A. R., 1992, *ApJ*, 397, 552
- Zijlstra A. A., 2004, *MNRAS*, 348, L23
- Zijlstra A. A., Loup C., Waters L. B. F. M., Whitelock P. A., van Loon J. T., Guglielmo F., 1996, *MNRAS*, 279, 32
- Zijlstra A. A. et al., 2004, *MNRAS*, 352, 325

This paper has been typeset from a  $\text{\TeX}/\text{\LaTeX}$  file prepared by the author.